Nonlinear Analysis of BVAM Model using Perturbation Techniques

By

Ahsan Naseer

00000317712

Supervisor

Dr. Imran Akhtar

Department of Mechanical Engineering

College of Electrical and Mechanical Engineering (CEME)

National University of Sciences and Technology (NUST)

Islamabad, Pakistan

March 2023

Nonlinear Analysis of BVAM Model using Perturbation Techniques

By

Ahsan Naseer

00000317712

Supervisor

Dr. Imran Akhtar

A thesis submitted in conformity with the requirements for the degree of *Master of Science* in Mechanical Engineering

Department of Mechanical Engineering

College of Electrical and Mechanical Engineering (CEME)

National University of Sciences and Technology (NUST)

Islamabad, Pakistan

March 2023

Declaration

I, *Ahsan Naseer* declare that this thesis titled "Nonlinear Analysis of BVAM Model using Perturbation Techniques" and the work presented in it are my own and has been generated by me as a result of my own original research.

I confirm that:

1. This work was done wholly or mainly while in candidature for a Master of Science degree at NUST
2. Where any part of this thesis has previously been submitted for a degree or any other qualification at NUST or any other institution, this has been clearly stated
3. Where I have consulted the published work of others, this is always clearly attributed
4. Where I have quoted from the work of others, the source is always given. With the exception of such quotations, this thesis is entirely my own work
5. I have acknowledged all main sources of help
6. Where the thesis is based on work done by myself jointly with others, I have made clear exactly what was done by others and what I have contributed myself

---

Ahsan Naseer,
00000317712

Language Correctness Certificate

This thesis has been read by an English expert and is free of typing, syntax, semantic, grammatical and spelling mistakes. Thesis is also according to the format given by the university.

Signature (Student): _____

Ahsan Naseer,

00000317712

Signature (Supervisor): _____

Dr. Imran Akhtar

Copyright Notice

Acknowledgments

Beginning with the name of Allah, the most loving, merciful and beneficent. I am thankful to my Creator who guided and enabled me doing my thesis. I am thankful to my supervisor Dr. Imran Akhtar from whom I have learnt how to do research and for nourishing my analytical abilities. I express my gratitude to my GEC committee members Dr. Zafar Abbas Bangash, Dr. Imran Raouf and Dr. Rashid Naseer for doing critical analysis of my research. Lastly I am thankful to my friends and course-mates for being there with me during my studies.

This thesis is dedicated to *my beloved mother*

Abstract

The bio-electric activity of the heart can be modeled by Barrio-Varea-Aragon-Maini (BVAM) model. This model covers normal rhythm and four arrhythmia that lie in the chaotic region. This model exhibits several bifurcations, starting from fixed point bifurcation, Hopf bifurcation, period doubling and ultimately leading to chaos. An analytical solution to the BVAM model is developed in the local region of Hopf bifurcation. Center manifold reduction is applied to the main governing equations to reduce the order of the system to limit cycle oscillations of center manifolds. Application of the method of multiple scales is used on the center manifolds to develop a normal form of Hopf bifurcation, which is then transformed back into the original coordinates. Comparison with the numerical solution shows that the analytical solution matches well with the numerical solution in the local region of the bifurcation. The value of the control parameter for period doubling bifurcation is identified using the Floquet multipliers of the monodromy matrix for the corresponding periodic solution. Shooting method is employed to get monodromy matrix and form periodic and period doubling cycle. It identifies periodic solution by iterating through the time period and initial conditions. The results of this research can be used for sensitivity and parametric analysis. Such solutions also allow simpler and low cost simulators for training and research purposes.

Keywords: *Bio-electric activity of the heart, Center Manifold Reduction, BVAM model, Bifurcations, Method of Multiple Scales*

Contents

List of Figures

List of Tables

List of Abbreviations and Symbols

Abbreviations

ECG	Electrocardiograms
MMS	Method of Multiple Scales
EKG	Electrocardiograms
NUST	National University of Sciences and Technology
CEME	College of Electrical and Mechanical Engineering

Chapter 1

Introduction

1.1 Dynamical Systems

All natural phenomena are nonlinear in nature. From the change of weather, the flow of fluids over different surfaces, the working of different engines to the beating of hearts, and many more. Nonlinear systems are inherently complex and finding their solution is often difficult. There are certain characteristics associated with nonlinear phenomena. These characteristics can be forming a limit cycle in any given space, frequency manipulation, aperiodic solution, and exhibiting chaotic behavior. In a nonlinear system, the change of output or state variable is generally not proportional to the input.
In mathematics, nonlinear systems are represented by a set of differential equations with at least one equation with more than one degree. The degree of an equation is defined to be the highest exponent of a given differential equation.

1.1.1 Types of Solution

A nonlinear equation is often difficult to solve. Many types of solutions exist for linear or nonlinear differential equations. This solution can be mainly classified into numerical solutions and analytical solutions. A numerical solution generally consists of an algorithm, an iterative scheme, or some set of sequence of rules, which when applied to any given set of a linear or nonlinear differential equation, shows a solution of the system. A numerical solution can only be visualized in a given phase space instead of an equation form. The problem with the numerical solution is that it has to be run over and over again to find the solution for different times, parameters, and initial and

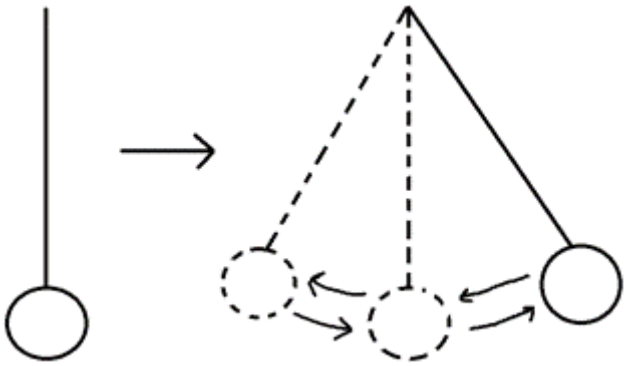

Figure 1.1: A schematic of simple pendulum as an example

boundary conditions. In any iterative numerical solution, the accuracy of a numerical solution depends upon the step size of time or any other spatial parameter and hence the number of iterations. If one wants to find an accurate solution, he will have to do more iterations, and therefore more time will be needed to solve for just one instance. A solution in any given algebraic functional form is known to be the analytical solution. For example, equation (1.1.1) shows a general representation of an analytical solution. If the state variable of an equation is y which is time t dependent any function functional form f dependent on the state variable, time, and some combination of parameters c can be taken as the analytical solution

$$y(t) = f(y, t, c). \tag{1.1.1}$$

The analytical solution, as opposed to the numerical solution, is difficult to find and in many cases of complex nonlinear systems and even some linear systems, an analytical solution is not possible. Of course, there are benefits to going with the difficulty of finding an analytical solution that gives the upper hand to it. The benefits of the analytical solution will be discussed in the later sections. That is why wherever possible, it is best to find the analytical solution to the system. The simple pendulum has a general governing equation given in equation (1.1.1),

$$\frac{d^2u}{dt^2} + \frac{g}{l}u = 0 \tag{1.1.2}$$

and considering the case of a simple linear pendulum. A simple pendulum consists of a bob of definite mass and is connected to a very little mass of rod that is attached to a point from its other side. A pendulum is free to rotate on its axis. The solution of this

system oscillates around a fixed point or an equilibrium point. This oscillation is back and forth and the diminishing of amplitude with time is very small which many times in mathematics can be neglected.

$$u(t) = u_0 \cos \sqrt{\frac{g}{l}}\, t \tag{1.1.3}$$

A solution to this linearized system can be represented by a cosine function. It is dependent upon initial condition u_0, length of rod l and gravity g. This is the analytical solution to a pendulum problem. This solution develops an understanding of the nature of the system. For example in analytical solution terms with time t, is the angular frequency $\omega = \sqrt{\frac{g}{l}}$ and its inverse is the time period $T_0 = 2\pi\sqrt{\frac{l}{g}}$. That is the benefit of an analytical solution. It establishes the fact that for a linear system, the only important parameters for the time period of the pendulum are gravity and the length of the pendulum rod. For a numerical solution, one has to break the differential time step into discrete steps and iterate over time to have its solution. The accuracy of a solution depends upon the size of the discrete steps

$$\frac{du}{dt}|_n = \frac{u_{n+1} - u_n}{t_{n+1} - t_n} \tag{1.1.4}$$

$$\frac{d^2u}{dt^2}|_n = \frac{\frac{du}{dt}|_{n+1} - \frac{du}{dt}|_n}{t_{n+2} - t_n}. \tag{1.1.5}$$

1.1.2 Tools of Nonlinear Dynamics

A very basic approach to visualizing a solution is visualizing in time series. In a time series plot, the state variable is plotted against time. This plot shows the state variable value at any past, present, and future instance of time. An example plot is shown in figure (1.2). In a Poincare section, the trajectory of any dynamical system is sampled periodically. If there is a phase plane of n dimensions, then a $n-1$ dimension is taken, and its intersection is taken out with the trajectory in the phase plane periodically. This in turn transforms a periodic solution into a fixed point solution. An example plot is shown in figure (1.3). In figure (1.3), the section $\sum$ is the Poincare section, and Q_k and Q_{k+1} are the intersection points of the trajectory in the specified phase space with the section $\sum$ which appears as dots on the Poincare section. The power spectrum of a time series describes how power is distributed across the frequency components that make up

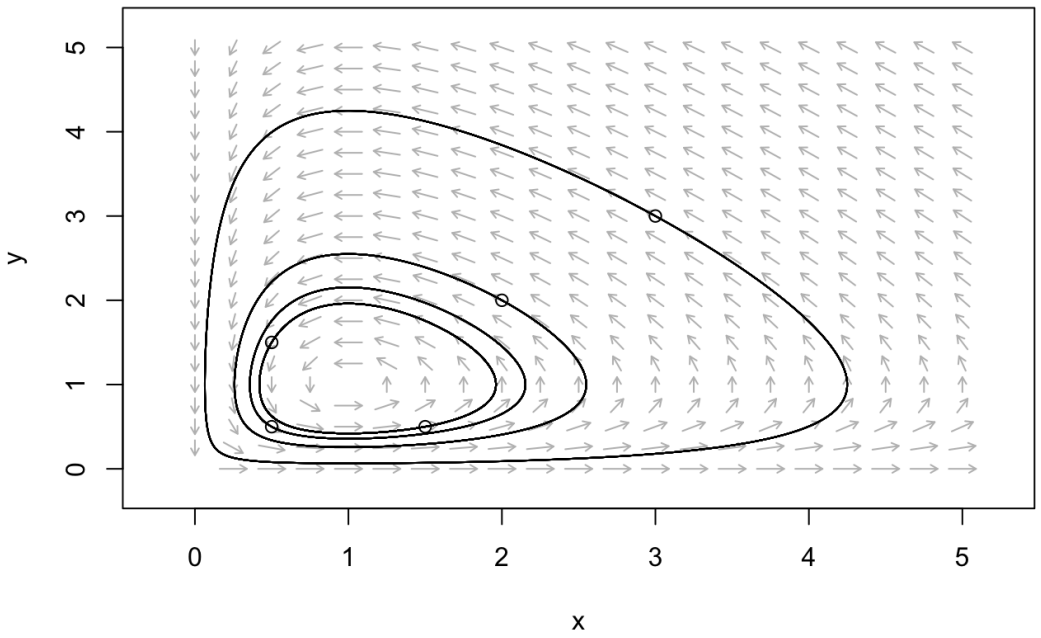

Figure 1.2: An example of phase portrait plots

the signal. Any physical signal can be decomposed into several discrete frequencies or a spectrum of frequencies over a continuous range using Fourier analysis. The spectrum is the statistical average of a signal or type of signal (including noise) as analyzed in terms of frequency content. An example plot is shown in figure (1.4).

1.1.3 Nature of Solution

There are multiple types of solutions for a system solely dependent upon time. These solutions include fixed point solutions, periodic solutions, multiple-period solutions, quasi-periodic solutions, and in many cases chaotic solutions.

A fixed-point solution or an equilibrium solution is a type of solution with a non-varying steady state against time. In any phase portrait, the trajectory of this kind of solution always approaches a fixed point with initial conditions provided in its proximity. An example of such a case includes a real pendulum that after some oscillations approaches an equilibrium point. In many situations temperature across the room or of an object assumes a constant steady state value providing a fixed point or equilibrium solution.

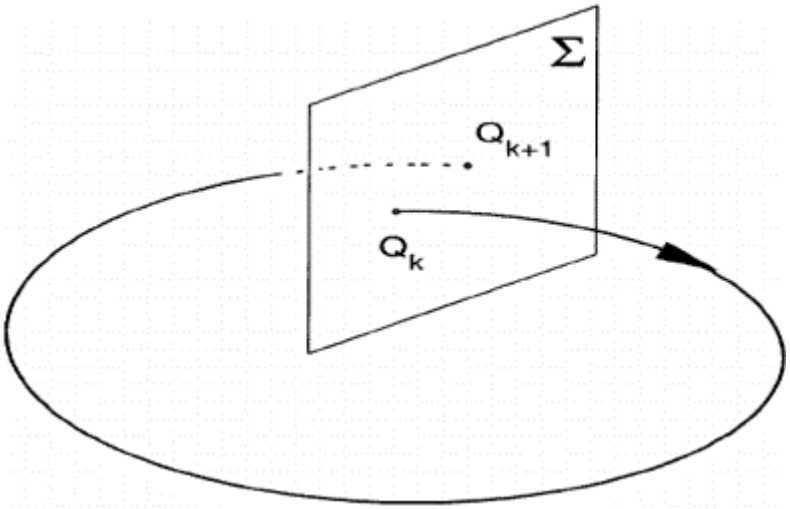

Figure 1.3: An example of Poincare sections

There is a class of dynamic solutions in which the physical state changes with time even in the steady state condition. Examples include the flutter of an aircraft wing, heart beatings, flows over surfaces, and many others. This type of solution can be further distinguished as a periodic solution or quasi-periodic solution. A periodic solution repeats itself over a constant period of time. The example includes an undamped pendulum, flutter, and wind turbine oscillations. The periodic solution can be a limit cycle oscillation (LCO). LCO is associated with nonlinear systems and it is defined to be an isolated steady close loop trajectory in phase space. The amplitude of the steady-state cycle is independent of the initial conditions. flutter is its pure example. The power spectrum of a periodic solution consists of the main harmonics and its odd or even harmonics or both. A periodic solution can be converted into a map. A single-period solution can be seen as a single dot on the Poincare section.

A periodic solution can have multiple periods. Beat is a phenomenon that contains multiple period oscillations. A two-period solution can have two distinct frequencies in the power spectrum. There is also a type of solution whose period changes after each cycle. These types of solutions are called quasi-periodic solutions or aperiodic solutions. The example includes the ECG of the normal rhythm of the heart. The Poincare section of a two-period solution has two dots on it. For a quasi-periodic solution, the Poincare section shows a close set of dots.

A distinct class of solutions for a deterministic system in which the predictability of the next instance does not be guaranteed. This type of solution comes under the category

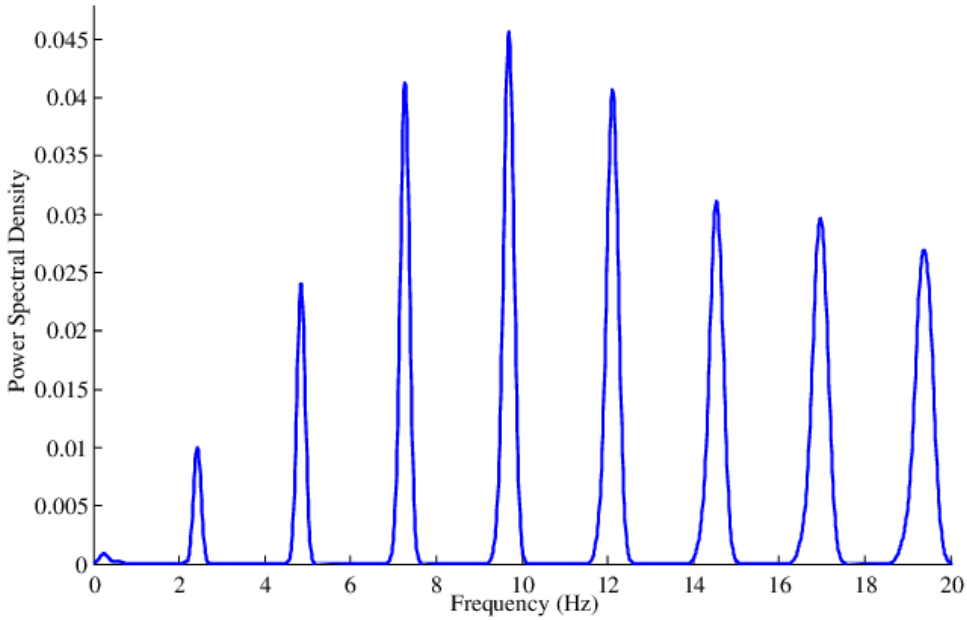

Figure 1.4: An example of power spectrum plots

of chaos. A chaotic solution is generally identified using the Lyapunov exponent. A Lyapunov exponent is the measurability of how two points in phase space which at time t=0 are very close to each other evolve with time. Lyapunov exponent is the slope of the difference between the two initial conditions close to each other evolving in time.
In a normal periodic or aperiodic solution with LCO, two initial conditions close to each come further close and eventually come to the same point or trajectory in case of a stable solution. However, in the case of a chaotic solution, this difference increases but is bounded in time. Therefore, the Lyapunov exponent of the chaotic solution is positive.

1.2 Mechanical System of the Heart

The human heart is an important biological organ making life possible for human beings. It primarily acts as a pump propelling blood to the whole body. Like any other pump, it is actuated by electrical pulses in the form of action potential driving the overall four chambers of the heart. Two of these chambers are called atria classified as the left and right atrium and two are the ventricles which are situated at the bottom of the atria.
The heart is a combination of two pumps. The left side of the heart consisting of the

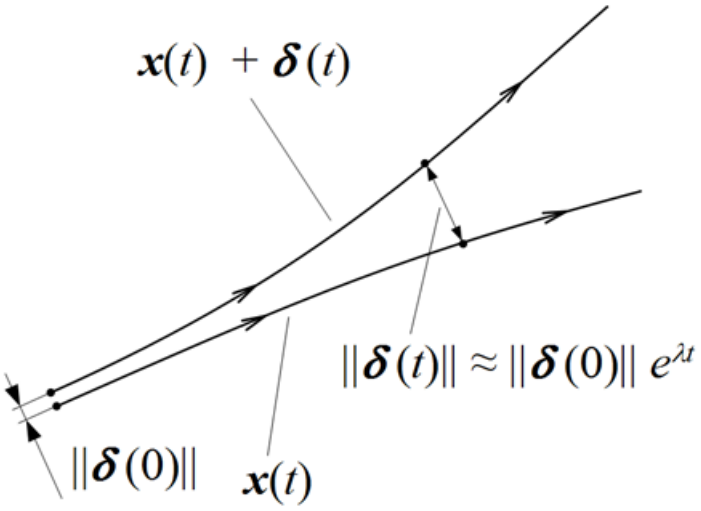

Figure 1.5: Two trajectories in phase space from nearby initial conditions for understanding Lyapunov exponent

left atrium and left ventricle forms one of the pumps and the other pump consists of the right atrium and right ventricle. The right pump of the heart pumps de-oxygenated blood to the lungs where it is oxygenated and transferred to the left side pump of the heart. The left side heart then propels the blood to the whole body.

Each atrium serves as a weak priming pump for the ventricle, assisting in the movement of blood into it. The ventricles then provide the major pumping power that drives blood either via the pulmonary circulation or the systemic circulation, depending on which ventricle is used. The pericardium, a two-layer sac that covers and maintains the heart in place, surrounds the heart. The heart's special processes create a continuous series of contractions known as cardiac rhythmicity, which is caused by action potentials being sent all the surface of the cardiac muscle and causing the heart's rhythmical beat. Atrial muscle, ventricular muscle, and specific excitatory and conductive muscle fibers are the three basic kinds of cardiac muscle found in the heart. The atrial and ventricular forms of muscle contract in a similar fashion to skeletal muscle, but for a considerably longer period of time since the heart is highly specialized excitatory and conductive fibers. Instead of contractile fibrils, they have automatic rhythmical electrical discharge in the form of action potentials or conduction of action potentials through the heart, giving an excitatory system that governs the heart's rhythmical beating.

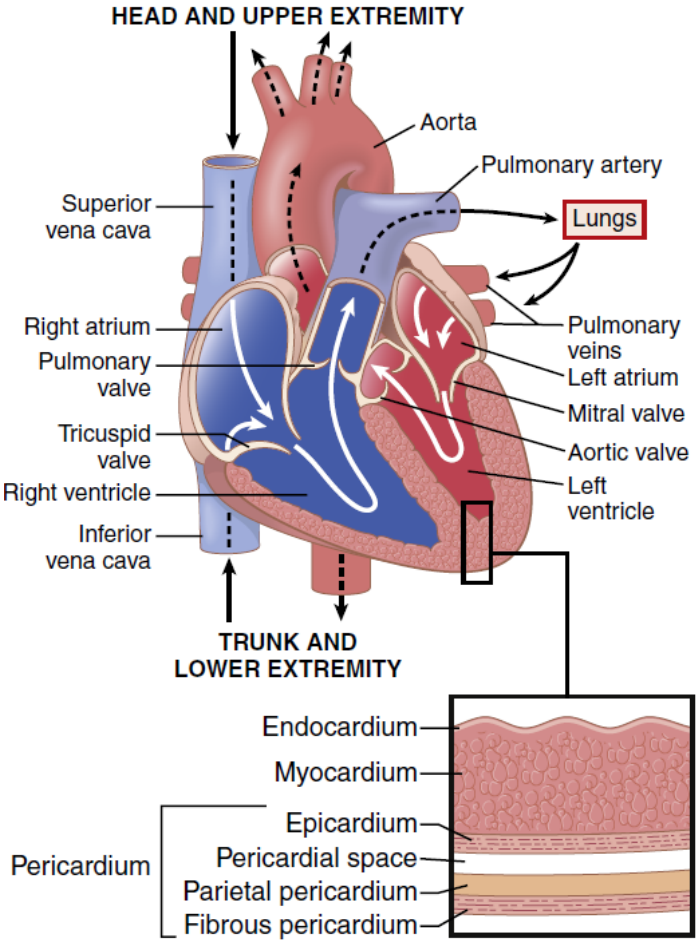

Figure 1.6: Mechanical anatomy of heart [1]

Blood flows continuously into the atria from the great veins; roughly 80% of blood flows directly through the atria into the ventricles, even before the atria contract. Following that, atrial contraction normally results in a 20% filling of the ventricles. The atria act as priming pumps, increasing the efficacy of ventricular pumping by up to 20%. The heart, on the other hand, can continue to function under most settings even without this extra 20% efficacy since it can routinely pump 300 percent to 400 percent more blood than the resting body requires. If the atria fail to function, the difference is unlikely to be recognized unless a person exercises; at that point, symptoms of heart failure, including shortness of breath, may appear.

The opening of the valves is not audible while listening to the heart with a stethoscope since it is a rather gradual operation that generally creates no noise. When the valves close, however, the vanes of the valves and the surrounding fluids shake due to abrupt pressure changes, causing the sound to flow in all directions through the chest. The

closing of the AV valves causes a sound when the ventricles contract. The initial heart sound is characterized by a low vibration pitch and a relatively long duration (S1). Because the aortic and pulmonary valves close quickly towards the conclusion of systole, one hears a sudden snap and the surroundings shake for a brief duration. The second heart sound is the name given to this sound (S2).
The heart only pumps 4 to 6 liters of blood per minute while a person is at rest. The heart may pump four to seven times this amount during vigorous activity. The primary processes for controlling heart pumping are (1) intrinsic cardiac pumping regulation in response to variations in blood flow into the heart; and (2) autonomic nervous system control of heart rate and heart strength.

1.3 Electrical System of the Heart

The human heart is also an electrical oscillator exhibiting strong nonlinear behavior. As discussed before specialized excitatory and conductive muscle fibers are the muscle of the heart that produce or conduct electrical pulses. There are three primary nodes where these pulses originated. These three nodes govern the perfect contraction and expansion of the heart along with pumping blood. These nodes are known as sinoatrial (SA) nodes located at the upper side of the atrium. The pulse originating here spreads over the atrium valves and produces heart contraction. Then there is the atrioventricular (AV) node which is located between the atrium and ventricle and is responsible for initiating the excitation of the ventricle and also providing a delay to the start of ventricle contraction in a cycle during the contraction of the atrium. Purkinje fibers conduct the electrical pulses through the ventricles of the heart and are responsible for uniform contraction of ventricles with no delay between the start and portion of the ventricle.

1.3.1 Action Potential in Cardiac Cycle

The action potential climbs from a highly negative value of around -85 millivolts between beats to a slightly positive value of about +20 millivolts during each beat, as illustrated in figure (1.8). After the first spike, the membrane stays depolarized for roughly 0.2

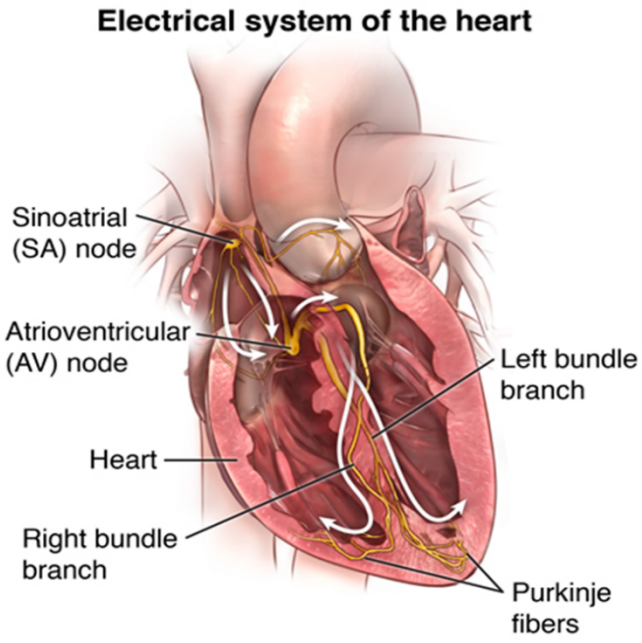

Figure 1.7: Electrical anatomy of the heart

seconds, forming a plateau, which is followed by rapid repolarization at the end of the plateau. The existence of this plateau in the action potential allows cardiac muscle contractions to persist up to 15 times longer than skeletal muscle contractions.

The extended action potential and plateau in cardiac muscle are due to at least two main changes in membrane characteristics between cardiac and skeletal muscle. First, the action potential of skeletal muscle is nearly entirely triggered by the abrupt opening of a large number of fast sodium channels, which enable massive amounts of sodium ions from the extracellular fluid to enter the skeletal muscle fiber. Fast channels are so named because they are only active for a few thousandths of a second before quickly closing. Repolarization happens at the conclusion of this closure, and the action potential is over in less than a thousandth of a second.

The opening of two types of channels in cardiac muscle causes the action potential to be triggered: A unique population of L-type calcium channels (slow calcium channels), also known as calcium-sodium channels, and voltage-activated rapid sodium channels comparable to those found in skeletal muscle are one way. This second class of sodium channels differs from fast sodium channels in that they take longer to open and, more importantly, they stay open for several tenths of a second. During this time, a large

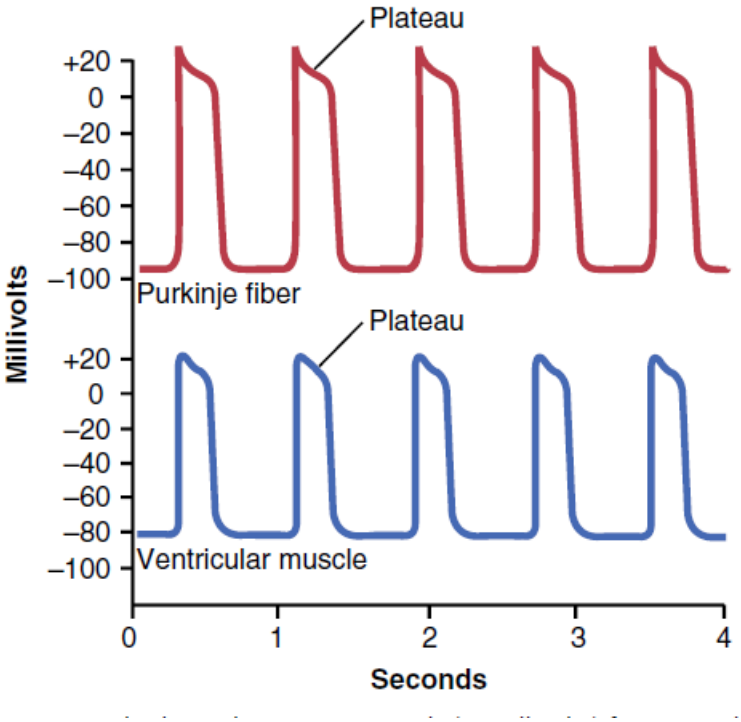

Figure 1.8: Acton potential [1]

number of calcium and sodium ions move through these channels to the interior of the heart muscle fiber, resulting in a prolonged period of depolarization and a plateau in the action potential. Furthermore, calcium ions coming during this plateau phase stimulate the muscle contractile process, whereas calcium ions driving skeletal muscle contraction originate from the sarcoplasmic reticulum inside the cell. Regardless of the source, lower potassium permeability reduces the outflow of positively charged potassium ions during the action potential plateau, preventing the action potential voltage from returning to its resting level too soon. When the slow calcium-sodium channels close after 0.2 to 0.3 seconds and the input of calcium and sodium ions stops, the membrane permeability for potassium ions rapidly rises. The quick loss of potassium from the fiber causes the membrane potential to revert to its resting level, thus stopping the action potential. Lower potassium permeability, regardless of the source, lowers the outflow of positively charged potassium ions during the action potential plateau, preventing the action potential voltage from recovering too quickly to its resting state. The membrane permeability for potassium ions rapidly rises when the sluggish calcium-sodium channels close after 0.2 to 0.3 seconds and the input of calcium and sodium ions ends. The action potential is stopped when potassium is rapidly lost from the fiber, causing the membrane potential

to return to its resting state.

1.3.2 Phases in Cardiac Cycle

Figure (1.9) summarizes the phases of the action potential in cardiac muscle and the ion flows that occur during each phase.
Phase 1- Depolarization: Sodium channels open quickly. The membrane potential becomes more positive as the cardiac cell is activated and depolarized. Fast sodium channels (voltage-gated sodium channels) open and allow sodium to flow quickly into the cell, depolarizing it. Before the sodium channels close, the membrane potential reaches roughly +20 millivolts.
Phase 2- Initial repolarization: The sodium channels close quickly. When the sodium channels close, the cell repolarizes, and potassium ions exit through open potassium channels.
Phase 3- Calcium channels open: The potassium channels are closing with the enhanced calcium ion permeability and decreased potassium ion permeability, the action potential plateaus after a brief initial repolarization. During phases 1 and 0, the voltage-gated calcium ion channels slowly open, allowing calcium to enter the cell. Potassium channels then shut, causing the action potential to plateau due to a combination of decreased potassium ion outflow and increased calcium ion inflow.
Phase 4- Rapid repolarization: Calcium channels close and potassium channels open slowly. The plateau is broken and the cell membrane potential is restored when calcium ion channels are closed and potassium ion permeability is enhanced, allowing potassium ions to depart the cell quickly.
Phase 5- Resting membrane potential: It has an average of about -80 to -90 millivolts.

1.4 Cardiac Cycle

The cardiac cycle is the series of events that occur from the beginning of one heartbeat to the beginning of the next. Each cycle is initiated by the spontaneous generation of an action potential in the sinus node, as previously indicated. The action potential goes

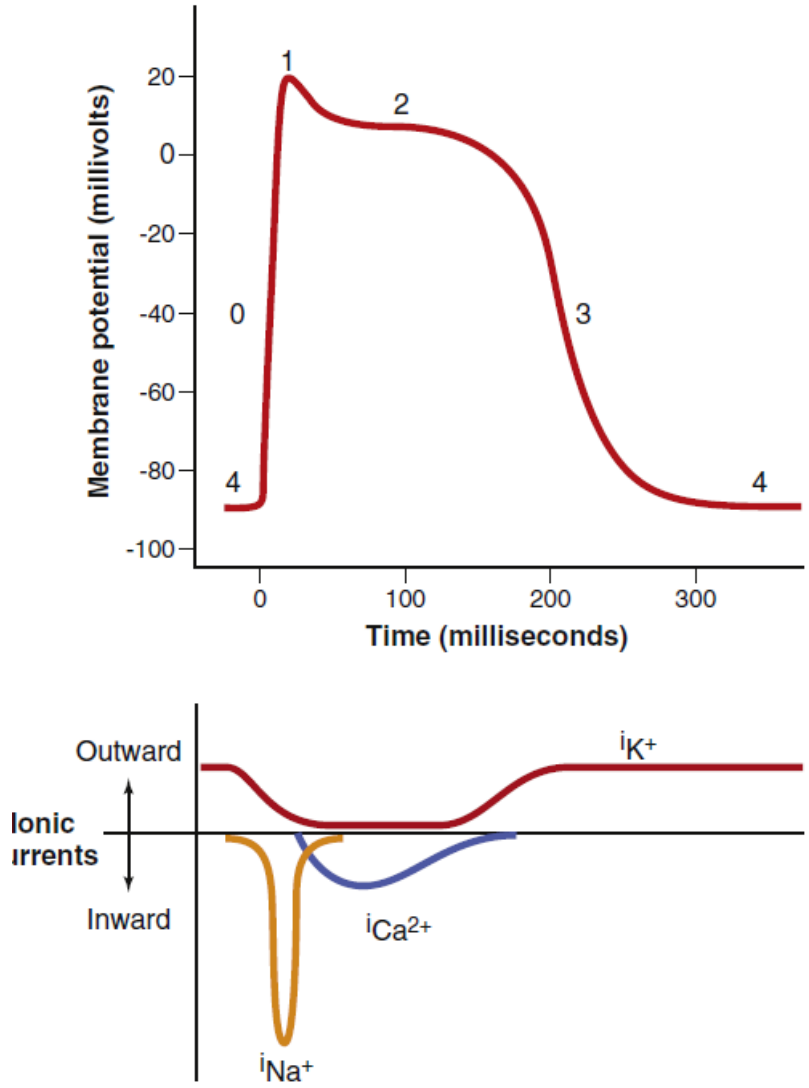

Figure 1.9: Phases of action potential [1]

quickly from here via both atria and then through the AV bundle into the ventricles, as it is located at the entrance of the superior vena cava in the superior lateral wall of the right atrium. Because of the peculiar arrangement of the conducting system from the atria to the ventricles, there is a delay of more than 0.1 second during the transit of the cardiac impulse from the atria to the ventricles. The atria contract first, enabling blood to flow into the ventricles before the forceful ventricular contraction occurs. The atria act as priming pumps for the ventricles, which provide the principal source of energy for blood flow throughout the body's circulatory system.

Figure (1.10) shows the P, Q, R, S, and T waves on the EKG. These are electrical voltages generated by the heart and detected by an ECG from the body's surface. The

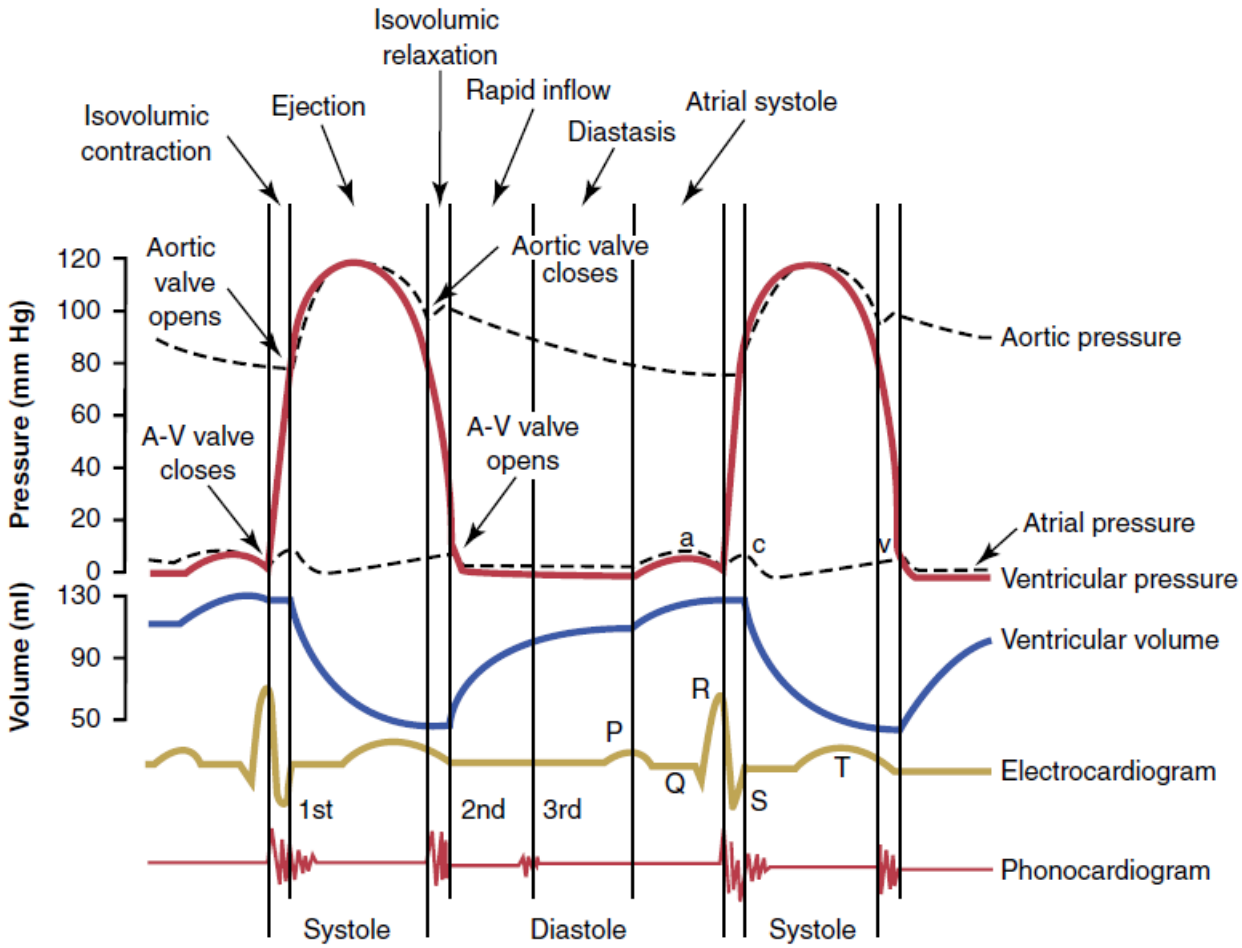

Figure 1.10: Comparison of pressure-volume inside the heart with ECG [1]

P wave is created when depolarization propagates throughout the atria, followed by atrial contraction, which generates a little rise in the atrial pressure curve shortly after the electrocardiograph P wave. Due to electrical depolarization of the ventricles, which causes the ventricles to contract and the ventricular pressure to rise, the QRS waves appear 0.16 second after the P wave begins. The QRS complex begins earlier than ventricular systole. Finally, during repolarization, the ventricular T wave signals the point at which the ventricular muscle fibres begin to relax. Therefore, the T wave appears just as ventricular contraction comes to a close.

1.4.1 Rhythmical Excitation of Cardiac Muscles

The average daily frequency of the human heart's rhythmic self-excitation and repeated contraction mechanism is 100,000, or 3 billion times throughout a lifetime. This amazing

accomplishment is made possible by a mechanism that carries out the following tasks. It generates electrical signals, which are swiftly transported throughout the heart and cause the cardiac muscle to contract rhythmically. When this system is functioning correctly, the atria compress approximately a sixth of a second before the ventricles, enabling the latter to fill before pumping blood through the lungs and peripheral circulation.

The system's ability to enable all ventricle regions to almost entirely constrict concurrently is another crucial component for generating the best possible pressure in the ventricular chambers. Heart illness, particularly ischemia brought on by insufficient coronary blood flow, can damage the heart's rhythmical and conductive system. The abnormal cardiac beat or erratically sequenced contractions of the heart chambers can significantly impair the heart's ability to circulate blood, even to the point of mortality. The sinus node is a flattened, ellipsoid strip of specialized cardiac muscle that is around 3 mm in width, 15 mm in length, and 1 mm in thickness. It is in the superior posterolateral wall of the right atrium, immediately below and somewhat lateral to the superior vena cava's entry. This node's fibers have almost no contractile muscle filaments and are just 3 to 5 micrometers (m) in diameter, compared to the nearby atrial muscle fibers, which are 10 to 15 m in diameter. The atrial muscle fibers are immediately coupled to the sinus nodal fibers, thus any action potential initiated in the sinus node passes fast along the atrial muscle wall.

Self-excitation, a mechanism that causes automatic rhythmical discharge and contraction, is a capacity of some cardiac fibers. This is especially true of the heart's specialized conducting system, which includes sinus node fibers. The sinus node is usually in charge of the entire heart's beat rate.

1.4.2 Mechanism of Sinus Nodal Rhythmicity

Figure (1.10) displays three heartbeats of action potentials captured inside a sinus nodal fiber, as well as a single ventricular muscle fiber action potential for comparison. The resting membrane potential of the sinus node fiber is between -55 and -60 millivolts, while that of the ventricular muscle fiber is between -85 and -90 millivolts. Since sodium and calcium ions naturally seep through the cell membranes of the sinus fibers, there is less intracellular negativity. This is because some of the intracellular negativity is neutral-

ized by the positive charges of the sodium and calcium ions as they reach the cell.
In cardiac muscle, three types of membrane ion channels play important roles in creating voltage changes in the action potential. The three kinds of sodium channels include fast sodium channels, calcium channels (particularly L-type or "slow" calcium channels), and potassium channels. The rapid upstroke spike of the action potential observed in ventricular muscle is induced by opening the fast sodium channels for a few $10,000^{th}$ of a second due to the rapid entry of positive sodium ions into the interior of the fiber. Due to the delayed opening of the slow sodium-calcium channels, which lasts around 0.3 seconds, the ventricular action potential achieves a plateau. Finally, when potassium channels are activated, large amounts of positive potassium ions flow outward through the fiber membrane, restoring the membrane potential to its resting condition. Since the resting potential of these channels in the sinus nodal fiber is substantially lower. The nodal fiber has a voltage of only -55 millivolts compared to the ventricular muscle fiber's -90 millivolts, and its role is different from that of the latter. The fast sodium channels are typically inactivated or closed at a voltage of -55 millivolts. This is due to the fact that the deactivation gates on the interior of the cell membrane that close the fast sodium channels shut and remain closed if the membrane potential is less than approximately -55 millivolts for more than a few milliseconds. Only the sluggish sodium-calcium channels can open i.e. become active, resulting in an action potential. As a consequence, the atrial nodal action potential matures more slowly than the ventricular muscle's action potential. Instead of returning suddenly as seen in the ventricular fiber, the potential slowly returns to its negative condition when the action potential happens.

1.5 Conduction and Excitation Control inside the Heart

The cardiac impulse generally originates in the sinus node, as we discussed while discussing its genesis and transit through the heart. This is not the case in some unusual circumstances. Other regions of the heart, such as the AV nodal and Purkinje fibers, can also demonstrate intrinsic rhythmical excitation in the same way as the sinus nodal fibers.
The AV nodal fibers discharge at a rate of 40 to 60 times per minute when not triggered by an external source, whereas the Purkinje fibers discharge at a rate of 15 to

40 times per minute. The sinus node normally beats at a rate of 70 to 80 times per minute, therefore these rates are unusual. Why is the sinus node in charge of the heart's rhythmicity rather than the AV node or the Purkinje fibers? The sinus node's discharge rate is far quicker than the AV node or Purkinje fiber's natural self-excitatory discharge rate, which explains why. When the sinus node fires, an impulse goes to the AV node and Purkinje fibers, where excitable membranes are discharged. Before the AV node or Purkinje fibers reach their self-excitation limitations, the sinus node discharges again. Therefore, before either of these locations can self-excite, the new impulse from the sinus node discharges both the AV node and the Purkinje fibers. The sinus node governs the heart's beat because its rate of rhythmical discharge is quicker than any other component of the heart. Therefore, the sinus node is almost always the heart's pacemaker in a healthy heart.

1.5.1 Ectopic Pacemaker (EP)

In some circumstances, the sinus node is surpassed by another area of the heart in terms of rhythmical release rate. Such growth may take place, for instance, when the Purkinje fibers or AV node behave abnormally. In either scenario, the sinus node is replaced by the AV node or the stimulated Purkinje fibers as the heart's pacemaker. Rarely, an area of the atrial or ventricular muscle experiences abnormal activity and takes on the role of the pacemaker.

EPs are those that are located away from the sinus nerve. An EP causes the heart's various chambers to beat in an abnormal pattern, which can seriously impair the heart's ability to circulate blood.

Another reason for the pacemaker to move is an obstruction of the cardiac impulse's path from the sinus node to the rest of the heart. The new pacemaker is usually seen at the AV node or in the entering region of the AV bundle as it travels to the ventricles. When the AV nodal and bundle system fails to transmit the cardiac impulse, a new pacemaker emerges in the Purkinje system of the ventricles, moving the ventricular muscle at a new rate, typically between 15 and 40 pulses per minute. The atria continue to beat at the sinus node's normal rate. The Purkinje system does not start producing its normal rhythmical impulses until 5 to 20 seconds after an abrupt AV

bundle block because the Purkinje fibers had been "over-driven" by the rapid sinus impulses before the obstruction and were muted. The ventricles stop moving blood during these 5 to 20 seconds, and the individual passes out during the first 4 to 5 seconds of insufficient blood flow to the brain. The delayed recognition of the pulse is referred to as Stokes-Adams syndrome. A delay that lasts longer than usual may result in mortality.

1.5.2 Role of the Purkinje Fibers for Contraction of the Ventricles

The Purkinje system's fast conduction allows the cardiac impulse to reach practically all parts of the ventricles in a short amount of time, with the first ventricular muscle fiber being excited 0.03 to 0.06 seconds before the final ventricular muscle fiber. This timing causes the entire ventricular muscle in both ventricles to contract at about the same moment and then continue contracting for another 0.3 seconds.
This synchronized form of contraction is required for effective pumping by the two ventricular chambers. If the cardiac impulse were to move slowly through the ventricles, most of the ventricular mass would contract before the rest, resulting in a significant reduction in the total pumping effect. Slow transmission does occur in some kinds of ventricular failure, and the pumping efficacy of the ventricles can be reduced by as much as 20% to 30%. Implantable cardiac re-synchronization devices are pacemakers that use electrical wires or leads that can be implanted into the cardiac chambers to restore proper timing between the atria and both ventricles in patients with enlarged and weaker hearts.

1.6 Electrocardiograms

The typical ECG shown in figure (1.11) consists of a P wave, a QRS complex, and a T wave. Although, not usually, the QRS complex is made up of three waves: the Q wave, the R wave, and the S wave.
Electrical potentials generated when the atria depolarize before cardiac constriction are what produce the P wave. Potentials created when the ventricles depolarize before contracting—specifically, as the depolarization wave spreads over the ventricles—are what

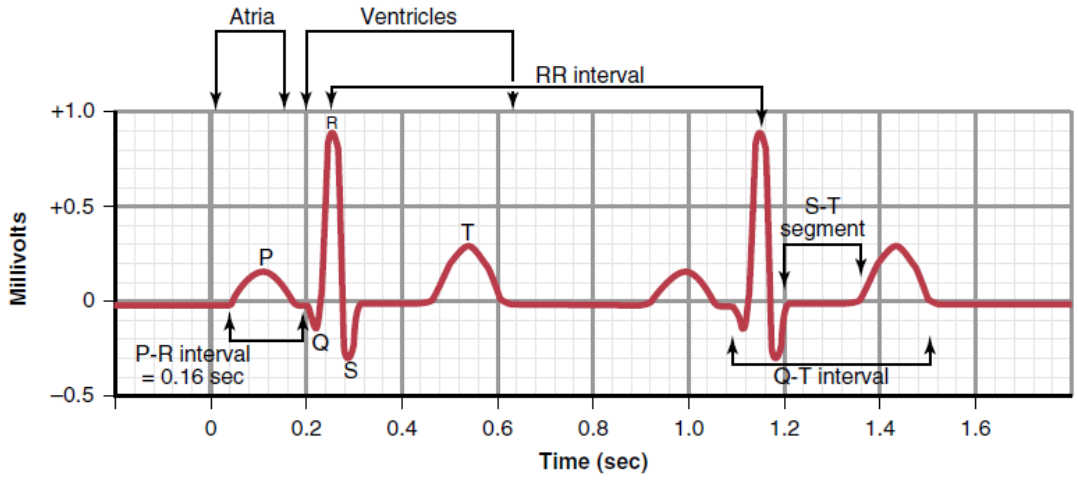

Figure 1.11: Electrocardiogram showing sinus rhythm [1]

give rise to the QRS complex. Consequently, the P wave and the QRS complex component are both depolarization waves. Potentials generated as the ventricles recoup from depolarization are what induce the T wave. This happens 0.25 to 0.35 seconds after the depolarization of the ventricular muscle. Repolarization wave is another name for the T wave.

The ECG contains both repolarization and depolarization waves. In electrocardiography, the difference between depolarization and repolarization waves is so important that it deserves an additional explanation.

1.6.1 Action Potential Link to QRS and T Waves

In the majority of instances, the monophasic action potential of the ventricular muscle lasts between 0.25 and 0.35 seconds. In figure (1.12), the upper panel displays a monophasic action potential recorded by a microelectrode inserted into a single cardiac muscle fiber. This action potential upsweeps in response to depolarization, but it descends in response to repolarization.

In figure (1.12), the lower half depicts a contemporaneous ECG recording from the same ventricle. The monophasic action potential has a T wave at its conclusion and QRS waves at its commencement. No potential is recorded on the ECG when the ventricular muscle is fully polarised or completely depolarized. Only when the muscle is

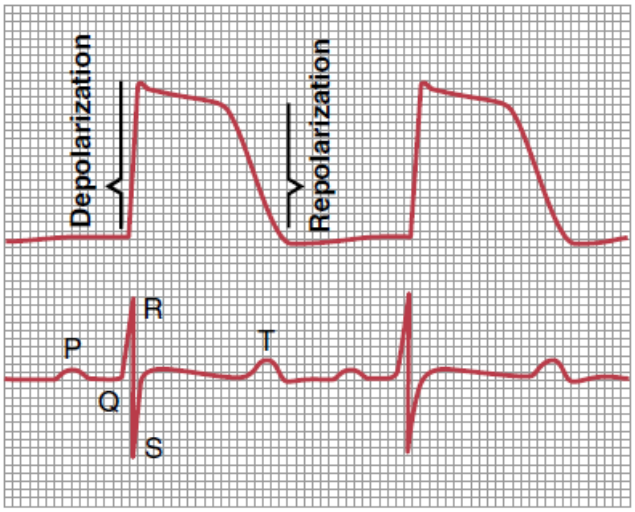

Figure 1.12: Normal rhythm ECG and action potential relationship [1]

partially polarised and partially depolarized can current travel from one region of the ventricles to another, and current spreads to the body's surface to create the ECG.

1.6.2 Relationship of Atrial and Ventricular Contraction to Electrocardiograms

Depolarization must enter the muscle and begin the molecular processes of contraction before muscular movement can happen. According to figure (1.12), the P wave appears at the start of the atrioventricular contraction and the QRS complex of waves appears at the start of ventricle contraction. The ventricles stay compressed up until re-polarization, or until the T wave has finished.

After the P wave has finished, the atria repolarize for 0.15 to 0.20 seconds, during which time the QRS complex is captured on the ECG. As a consequence, the much bigger QRS complex frequently covers up the atrial repolarization wave, also known as the atrial T wave.

An atrial T wave on an ECG is uncommon. The ventricular repolarization wave is represented by the T wave in a normal ECG. In most cases, the ventricular muscle begins to repolarize 0.20 seconds after the commencement of the depolarization wave (the QRS complex), while it can take up to 0.35 seconds in certain fibers. Therefore, the process of ventricular repolarization takes a long time, about 0.15 seconds. While the T wave in a typical ECG is lengthy, its voltage is much lower than that of the QRS complex,

due in part to its length.

Chapter 2

Literature Review

2.1 ECG Based Classification for Arrhythmia

An ECG is often used to diagnose problems related to the heart due to its ease of use and lack of invasiveness. The electrical signal of each heartbeat, which is a blend of action impulse waveforms produced by distinct specialized cardiac tissues located in the heart, can be used to detect some of the disorders in the heart. In recent decades, several studies have been conducted to build automated ECG-based heartbeat classification systems. ECG signal preprocessing, heartbeat segmentation methodologies, feature description methods, and learning algorithms, as well as the most up-to-date ECG-based automated abnormalities heartbeat classification methods, are all discussed in the work [7]. Additionally, [7] covers some of the databases used to examine processes in ANSI/AAMI EC57:1998/(R)2008 (ANSI/AAMI, 2008), a well-known standard developed by the Association for the Advancement of Medical Instrumentation (AAMI). The most common abnormal heart rhythm and the leading cause of stroke is atrial fibrillation (AF). Ablation, which involves removing atria regions, is a mostly empirical procedure with a poor clinical success rate. A basic model for the propagation of activation wavefront over an an-isotropic structure that replicates the branching network of cardiac muscle cells is proposed in [8]. AF forms spontaneously when transverse cell-to-cell coupling decreases below a threshold value, as it does with age. The authors identified critical areas that are involved in the onset and maintenance of AF and ablating them. Because of the simplicity of model [8] arrhythmia risk can be calculated and the transversal cell-to-cell coupling threshold value can be expressed as a function

of model parameters. The number of critical areas capable of initiating and sustaining micro reentrant circuits decreases as the refractory period increases, lowering this threshold value. Ablation treatment and arrhythmic risk assessment might benefit from these scientifically testable predictions.

2.2 Mathematical Models for Generating Electrocardiograms

The heart beats around 2 to 3 billion times in a normal human life span. Arrhythmia occurs when the normal rhythm of the heart is interrupted, resulting in considerably faster and irregular beats, which can result in premature death in ill people. The move from a normal heartbeat to an arrhythmia entails a change from regular electrical wave conduction to irregular or turbulent wave conduction, making this a physics and math challenge. In clinical, experimental, and theoretical research over the last century, dynamical theories have been demonstrated to be critical in understanding the mechanisms underlying the genesis of both normal and deadly arrhythmia.

Zhilin Qu et al. [9] summarized the nonlinear and stochastic dynamics that occur in the heart, as well as their links to normal cardiac functions and arrhythmia, by integrating dynamics from the molecular (microscopic) scale to the organelle (mesoscopic) scale, to the cellular, tissue, and organ (macroscopic) scales. It is explained that the existing obstacles and challenges, as well as how multi-scale mathematical modeling and nonlinear dynamics might aid in the resolution of these issues. Aberrant cardiac excitation is caused by abnormalities and propagation blockages in the Purkinje circuit. Ventricular tachycardia and fibrillation, two of the most prevalent causes of sudden cardiac death, appear to be linked to the Purkinje network. Anatomically accurate modeling is becoming increasingly important in the research of heart arrhythmia. The Purkinje network is not described in the vast majority of available anatomical models. Therefore, these models cannot be used to investigate critical role of the Purkinje system in arrhythmia development and maintenance.

Tusscher et al. [10] summarized previous works on modeling the Purkinje system and reports on the creation of a Purkinje system for human ventricular model. Authors [10] replicated both normal and abnormal bundle branch block and reentry activation patterns using the model.

In a dynamical model [11], three coupled ordinary differential equations (ODE) are employed to generate realistic synthetic ECG signals. Furthermore, many of the morphological variations found in the human ECG are due to the geometrical structure of the model. PQRST-complex morphologies may differ depending on model parameters. The operator can alter the heart rate mean and standard deviation, the PQRST cycle shape, and the power spectrum of the RR tachogram. The model takes into account both high-frequency (HF) respiratory sinus arrhythmia and low-frequency (LF) Mayer waves, as well as the LF/HF ratio. The outcomes are QT dispersion and R-peak amplitude modulation, as well as a significant amount of beat-to-beat fluctuation in the structure and timing of the human ECG.

The RR-interval power spectrum can be chosen ahead of time and utilized to drive the ECG generator. The operator can then define heart rate dynamics like mean and standard deviation, as well as spectrum features like the LF/HF ratio. Furthermore, by defining the positions of the P, Q, R, S, and T events, as well as the magnitude of their influence on the ECG, the average morphology may be altered. When comparing different biological signal processing algorithms, the presence of a true ECG serves as a benchmark. It is vital to understand how these techniques work at varied noise levels and sample frequencies to test their operational features in a clinical setting.

A recent work [12] provides a deterministic model based on traditional map dynamics for modeling cardiac electrical activity. These models include nonlinearity, which represents the self-regulatory function of the heart. Signal processing approaches for physiological signals may be tested using synthetic electrocardiograph data based on deterministic chaos. The model is based on the standard map dynamics and may be enhanced by mixing two or more standard maps. To increase realism of the signal, stochastic effects can be incorporated. This method develops a formula for synthesizing ECG signals using deterministic chaos. These signals may be used to evaluate time series analysis algorithms using real ECGs as a baseline.It is worth mentioning that [12] ECG generation model is data-driven, meaning the equations were designed to generate actual ECG signals. Similarly, more complicated models based on the combination of physiological models for electrical heart activity and chaotic dynamics appear to be conceivable to create.

Angela et al. [13] investigated a phenomenological heartbeat model made up of two coupled van der Pol oscillators. This model accounts for both unidirectional and bidirec-

tional connections, as well as external driving from a pacemaker. Even when subjected to external forces or parameter mismatches, which are inescapable in a physiological context, both units should oscillate in lockstep to enable stable functioning. It investigated the synchronization characteristics of such a link in terms of coupling type and intensity. Authors were interested in employing chaotic oscillator frequency modulation to synchronize rhythms and it also investigated how unstable dimension variability in the chaotic invariant set might trigger shadowing breakdown of numerically generated chaotic trajectories of the connected oscillator system.

The reaction-diffusion equation predicts that wave propagation will result in medium deformation in many real-world situations. The coupled reaction-diffusion mechanics (RDM) are used to mathematically mimic such processes. The effects of deformation on wave propagation in cardiac tissue, often known as mechano-electrical feedback (MEF), were recently investigated using RDM systems. The findings of numerous of these studies, particularly those pertaining to the influence of deformation on pacemaker activity and spiral wave dynamics in the heart, are summarized in article [3].

A model of electrical activity in the heart [4] has been proposed that accurately reproduces real ECG signals in healthy people. Two resistance-inductor-capacitor (RLC) linear oscillators are used in the model, which is periodically triggered by the primary pacemaker impulses at the frequency of a genuine heart. The recommended model includes an electrical cardiac conduction system with a coupling capacitor that can be unidirectional or bidirectional, and the atria are represented by one oscillator and the ventricles by another. The main pacemaker activates a network of two capacitively connected oscillators regularly, pushing periodic limit cycles into the system; a time delay is added to mimic the electrical transit delay between the atria and the ventricles. Therefore, healthy synthetic ECG signals are formed by linearly combining the current signal of each oscillator. The electrical transport delay from the atria to the ventricles is represented by the first oscillator, which has a temporal delay. An analytical solution can be formed for a single impulse, and this solution was extended to an impulse train utilizing the superposition notion, which includes periodic forcing of limit cycles similar to what happens in the heart. The finding suggested that the proposed model may be utilized to simply depict the worldwide consequences of cardiac electrical activity. The ability of the proposed model to create analytical solutions is a significant feature. Different system parameters, such as the interplay between excitable oscillators, frequency and

coupling types, and the main pacemaker features, can also be examined to produce various harmful cardiac rhythms. Finally, in comparison to earlier models, their model was capable of extracting common characteristics and replicating the most essential waves found in real ECGs.

Another work [4] proposed a model of the cardiac conduction system made up of a network of heterogeneous oscillators characterized by nonlinear differential equations, such as main pacemakers and heart muscles. The SA node, AV node, and Purkinje system are represented by modified van der Pol-type oscillators with time-delay velocity coupling. Atrial and ventricular muscles are explained using a modified FitzHugh–Nagumo model, with depolarization and repolarization processes considered independent waves. The authors created synthetic ECG as a combined signal of atrial and ventricular muscles and utilized it to mimic a variety of normal and diseased rhythms. Researchers may use therapeutically relevant real ECG values to analyze pacemaker interactions and the consequent global heartbeat dynamics thanks to the inclusion of cardiac muscle response. This characteristic distinguishes the model from other cardiac oscillator models.

The model given in [4] is capable of reproducing realistic ECG patterns linked to well-known normal and abnormal rhythms. The findings suggest that the suggested model may be used to examine worldwide cardiac electrical activity. It enables researchers to investigate the interactions between basic components of the heart, with the option of employing many pacemaker models with various coupling types, as well as analyzing and comparing underlying cardiac dynamics to clinically used ECG patterns.

2.3 Classifying Ventricular Fibrillation

The academicians has been fascinated by the use of nonlinear time series analysis to determine whether or not the human heart system is chaotic for a long time. ECG and pulse pressure propagation data are insufficient to demonstrate the presence of deterministic chaotic dynamics in cardiac time series. Furthermore, with the exception of the most basic linear noise hypotheses, these approaches fail to rule out any but the most fundamental linear noise hypotheses. The study [14] describes a fourth technique for testing the assumptions of a noise-driven periodic orbit to see if the signals are consistent with deterministic chaos.

The algorithmic complexity is employed as the differentiating statistic in the surrogate data approach. The authors then utilized nonlinear modeling to forecast ECG and pulse data in the short term, demonstrating that the processes are predictable. The authors showed the use of those methodologies on human ECG recordings and blood pressure propagation at the fingertip of seven healthy people. According to their findings, bounded aperiodic determinism may be found in both ECG and pulse time series. It is difficult to tell if the underlying system is chaotic due to (unavoidable) dynamic noise.

Due to chaotic events, cardiac arrhythmia has been seen. A Ruelle-Takens-Newhouse path to chaos from regular rhythm causes ventricular fibrillation (VF), a kind of spatiotemporal chaos. An ectopic pacemaker that activated the ventricular muscle to reflect arrhythmia was postulated in [5] as part of a modified heterogeneous oscillator model of the cardiac conduction system. With this alteration, a single parameter governs the shift from normal rhythm to VF.

The expanded model includes an ectopic pacemaker connected to the ventricular muscles, which allows for the formation of VF, with the coupling constant serving as a control parameter. The ECG in VF becomes chaotic. Furthermore, when the control parameter is modified, the transition from a regular synchronized rhythm to a chaotic one follows the quasi-periodic, torus, or Ruelle-Takens-Newhouse path to chaos [5].

2.4 Normal Form of Governing Equations

The normal form is proposed as a method for evaluating the performance and reliability of piezo aeroelastic energy harvesters based on galloping. Two separate harvesting systems are being considered.

A multilayered cantilever beam is connected to a tip mass prismatic structure in the first design. Aerodynamic nonlinearity is the only source of nonlinearity in this system. Two cantilever beams are joined in the second arrangement by an equilateral triangular cross-section bar. The structural and aerodynamic nonlinearities of this system are deliberate. The authors created electromechanical controlling equations that link transverse displacement to generated voltage for both systems [15]. The effects of electrical load resistance and harvester type on the onset speed of galloping were studied using linear analysis. After that, the normal form of Hopf bifurcation was computed and uti-

lized to define the sort of instability that happens there.

Load resistance, cross-section shape (first harvester), and nonlinear torsional springs were all explored for their influence on the harvesters' performance and forms of instabilities (second harvester). The results demonstrated that the bigger the absolute value of the effective nonlinearity, the smaller the generated voltage and collected power are. Furthermore, for the first system, the Hopf bifurcation is supercritical, and both cross-sections are investigated. Supercritical or subcritical instabilities are obtained throughout a wide range of values in the second system, depending on structural nonlinearity. The range has been demonstrated to vary based on the electrical load resistance value in each situation. The advantage of employing the normal form of the Hopf bifurcation was found to identify the kind of instability and construct optimal and reliable energy harvesters.

2.5 Approximating the Heartbeat as Relaxation Oscillation and an Electrical Model of the Heart

The van der Pol oscillator is a single degree of freedom, second-order differential equation with cubic nonlinearity at the damping. This oscillator plays an important role in many applications, for example in simulating the action potential for any of the nodes of the heart or even forming the ECG of the whole cardiac cycle,

$$\frac{d^2v}{dt^2} - \alpha(1-v^2)\frac{dv}{dt} + \omega^2 v = 0, \tag{2.5.1}$$

this system (2.5.1), is unstable at $v = 0$ due to negative damping. Weak nonlinearity for example in figure (2.1a), shows the phase portraits for the simple oscillator given in equation (2.5.1). The term ϵ is the ratio of the coefficient of damping to stiffness i.e., $\epsilon = \frac{\alpha^2}{\omega^2}$. The phase portrait shows LCO for weak nonlinear terms. However, this phase portrait is a bit deformed when the strength of nonlinearity is increased for example $\epsilon = 1$ in figure (2.1b).

In figure (2.2) it is shown that the time series data for $\epsilon = 10$ shows strong nonlinear behavior. The nonlinear damping term plays an important role in the behavior of the system. The damping is both negative and positive as the amplitude of the system is steadily increased or decreased for amplitude $v < 1$ the damping is negative and it tends to make the system go away from zero and make it unstable. The slope of the trajectory

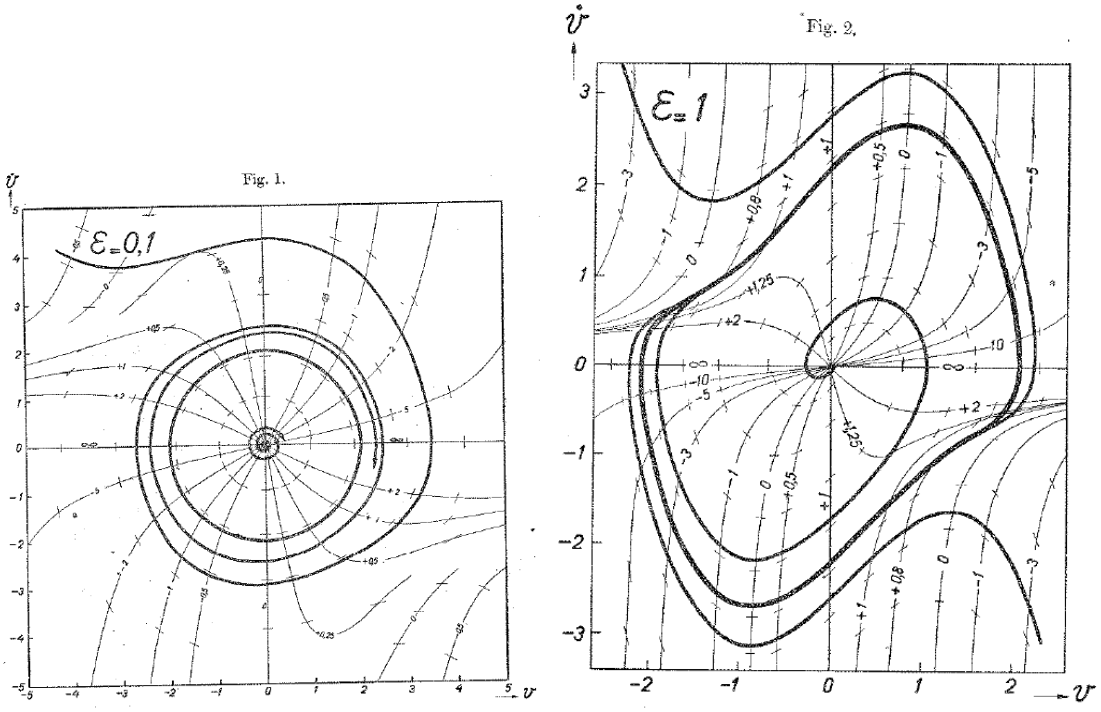

(a) van der pol oscillator at $\epsilon = 0.1$ (b) van der pol oscillator at $\epsilon = 1$

Figure 2.1: Phase portraits of van der Pol oscillator at different strength of nonlinearity [2]

with time increases as the amplitude rises. However, as the amplitude crosses ± 1, the damping term becomes positive and damping steadily increases with an increase in amplitude. It, therefore, stops the system at a particular value of magnitude for instance 2 in figure (2.2) and makes it decay however, as the trajectory in phase time space again crosses to less than $|1|$, again negative damping make it go away from the time axis. However, the strong nonlinear nature is exhibited by a simple nonlinear van der Pol oscillator of equation (2.5.1). This behavior is very similar to action potential form within a heart that is actuating the pumping action.

For applying a relaxation oscillator to the heart, the heart is considered as three degrees of freedom system. The three independent behavior is taken due to three nodes known as the SA node, atrioventricular node, and Purkinje muscles. A relaxation oscillator can be represented by an electrical circuit as shown in figure (2.3). Connecting three electrical oscillators as shown in figure (2.4) makes a coupled model representing the sinus, atrial and ventricular sections of the heart. The output can be seen in figure (2.5) closely resembles the ECG of the heart.

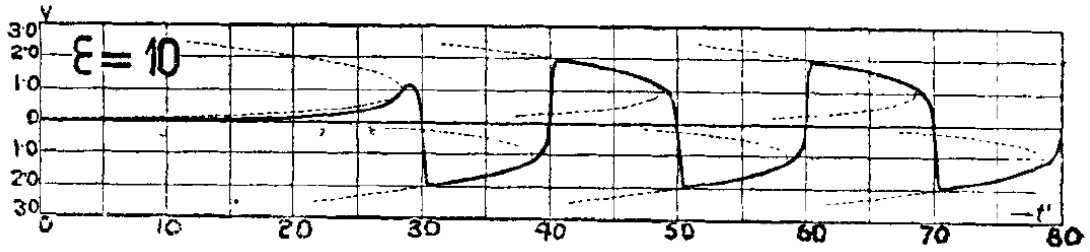

Figure 2.2: van der Pol oscillator time series profile at strong nonlinearity [2]

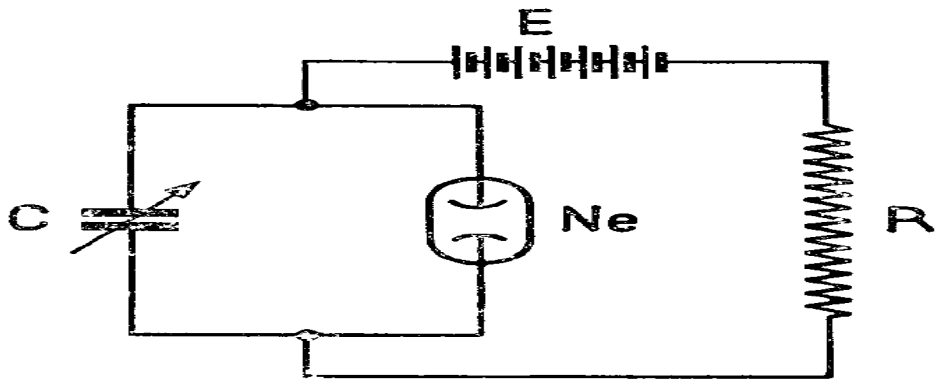

Figure 2.3: Electrical circuit model of equation (2.5.1) [2]

2.6 Describing Cardiac Mechano-electrical Feedback with Reaction-Diffusion Equations

The reaction-diffusion equation can model a wide variety of phenomena of biological importance. One of the applications is modeling the electrical and mechanical activity of the heart. In the dynamics of the heart, an electrical excitation initiates mechanical deformation. The types of tissues are different, some of the excitable tissues and some tissue are stretched activated channels (SAC). The SAC produces current when deformed, so there is feedback of mechanical deformation of the heart on its electrical activity. This mechano-electric feedback is present in the ECG of the heart.

Mechano-electric feedback has its application in the activity of the heart. The heart pacemakers usually produce current which controls or rehabilitates the normal activity of the heart. Electric shocks are executed on patients with very abnormal activity of the heart. Similarly, the mechanical impacts can vary the ECG of the heart.

A system of reaction-diffusion equations can be used to describe the electrical activity of the heart. Equations (2.6.1) is a common mono-domain model for the heart tissue.

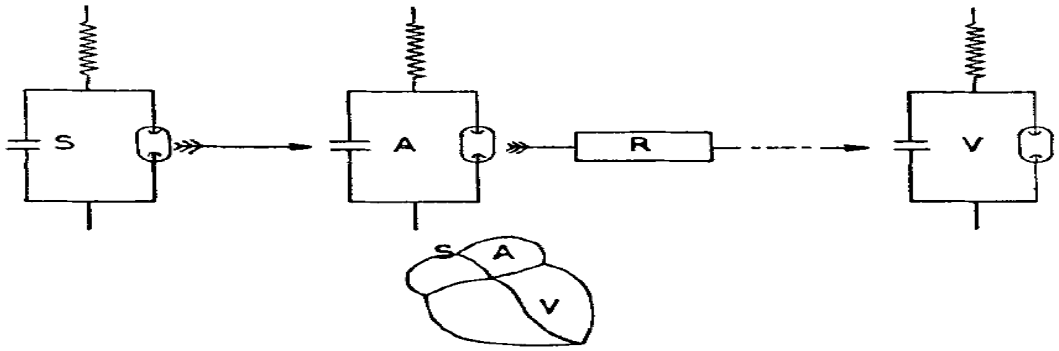

Figure 2.4: Three coupled electrical circuit model of equation (2.5.1) [2]

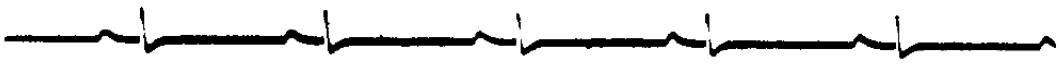

Figure 2.5: ECG of the heart using the van der Pol relaxation oscillator model [2]

The first equation describes changes in the cell membrane trans-membrane potential V (with capacitance C) due to inward and outward trans-membrane ionic currents I_m, as well as currents between adjacent cardiac cells $\Delta \cdot (\mathbf{D}\Delta V)$, where D is the conductivity tensor that accounts for the electrical anisotropy of the cell membrane.

$$\begin{aligned} C\frac{\partial V}{\partial t} &= \Delta \cdot (\mathbf{D}\Delta V) + I_m(V, g_i) \\ \frac{dg_i}{dt} &= \phi(g_i, V) \end{aligned} \tag{2.6.1}$$

The ionic current I_m is the total of all currents that flow across the cardiac membrane (e.g., $I_m = D + I_{Na} + I_{Ca} + I_K \ldots$) shown in figure (2.6). Each of these currents is dependent on other variables known as gating variables g_i, which account for the activation and inactivation kinetics of that specific current as measured experimentally. There are a variety of cardiac cell models available, each with its level of complexity and detail in the modeling of ionic currents I_m. Hodgkin-Huxley [16] and Noble [17] established the first biophysical or ionic models for nerve cells and cardiac cells respectively, which explain individual ion currents across the cell membrane based on extensive experimental findings. In addition to ionic currents, modern ionic models also describe concentration changes of the key ions involved. These models create correct cardiac action potential features such as shape, refractoriness, and rate dependency, as well as describe the multiple specific biophysical mechanisms of excitation that occur due to varied ion channel dynamics. These models frequently have a large number of ODEs (10-100) and are com-

putationally costly. Ionic models can be used to investigate the quantitative impacts of ion channels in a variety of settings, including drug development, and hereditary illnesses described in [18], [19] and [20]. Basic macroscopic features of the heart tissue, such as form, refractoriness, and so on, are described by more simplistic phenomenological models. These models have fewer ODEs (less than four) and can be used to investigate broader qualitative effects.

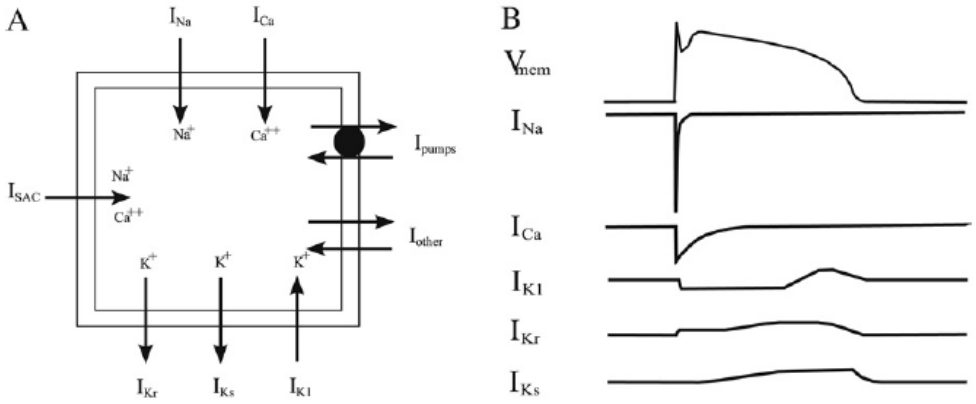

Figure 2.6: (A) Schematic overview of inward and outward ion currents across the surface cell membrane (B) Schematic time plot of currents during the action potential phase [3]

2.7 Determining Route to Chaos in Cardiac Conduction

A model of the electrical activity of the heart can be summed up in an ECG of the heart. Heart in normal condition has a specific ECG which has similar characteristics for every person. It has a PQRST waves feature which is positioned in a particular manner. The ECG of the person with the heart problem is not normal and can be classified as arrhythmia. One of the most malignant arrhythmia is known to be VF.
A normal rhythmic ECG of the heart can be modeled using a set of differential equations. There are two sections to the heterogeneous oscillator model of cardiac conduction suggested by Ryzhii et al. [21]. The first considers the primary pacemakers, the SA and AV nodes, as well as the Purkinje system (HP), which are represented by modified VDP oscillators, [22] with time delays, as proposed in [23]. A modified FitzHugh-Nagumo model [24] is used in the second section to describe the depolarization and re-polarization pro-

cesses in the atria and ventricles. The cardiac conduction system is characterized by seven sets of differential equations in this model, three of which are related to pacemakers and the other four to the heart muscles. As a combination of depolarization and re-polarization waves in the atrial and ventricular muscles, the model may generate synthetic ECG waveforms.

A modified van der Pol (VDP) oscillator is used to represent each natural heart pacemaker. A system of six differential equations with unidirectional time delay coupling describes the three natural pacemakers:

$$\begin{aligned}
\dot{x}_1 &= y_1 \\
\dot{y}_1 &= -a_1 y_1 (x_1 - u_{11})(x_1 - u_{12}) - f_1 x_1 (x_1 + d_1)(x_1 + e_1) \\
\dot{x}_2 &= y_2 \\
\dot{y}_1 &= -a_2 y_2 (x_2 - u_{21})(x_2 - u_{22}) - f_2 x_2 (x_2 + d_2)(x_2 + e_2) - k_{SA-AV}(y_1 - y_2) \\
\dot{x}_3 &= y_3 \\
\dot{y}_3 &= -a_3 y_3 (x_3 - u_{31})(x_3 - u_{32}) - f_3 x_3 (x_3 + d_3)(x_3 + e_3) - k_{SA-HP}(y_2 - y_3)
\end{aligned} \tag{2.7.1}$$

The synchronization required by the system is provided by two-time delay "velocity" or "current" couplings, established between pacemaker nodes in the system (2.7.1). The terms a_i, d_i, e_i, f_i and u_{ij} are the parameters of each oscillator, k_{SA-AV} and k_{AV-HP} are the coupling coefficients, $y_i^{\tau_n} = y_i(t - \tau_n)$ are the current coupling components, where τ_n are time delays and n refers to $AV - HP$ or $SA - AV$ couplings. The parameters f_1, f_2 and f_3 set the intrinsic frequencies of the natural pacemakers. The coupling coefficients must be proportional to f_1 [21] , thus for simplicity they are set as $k_{SAAV} = k_{AVHP} = f_1$.

A modified FitzHugh-Nagumo system [24] describes the electrical responses of the atria and ventricles muscles. A system of four sets of ODE is used to simulate the depolar-

ization and re-polarization processes in cardiac muscles:

$$
\begin{aligned}
\dot{z}_1 &= k_1(-c_1 z_1(z_1 - w_{11})(z_1 - w_{12}) - b_1 v_1 - d_1 v_1 z_1 + I_{AT_{De}}) \\
\dot{v}_1 &= k_1 h_1(z_1 - g_1 v_1) \\
\dot{z}_2 &= k_2(-c_2 z_2(z_2 - w_{21})(z_2 - w_{22}) - b_2 v_2 - d_2 v_2 z_2 + I_{AT_{Re}}) \\
\dot{v}_2 &= k_2 h_2(z_2 - g_2 v_2) \\
\dot{z}_3 &= k_3(-c_3 z_3(z_3 - w_{31})(z_3 - w_{32}) - b_3 v_3 - d_3 v_3 z_3 + I_{VN_{De}}) \\
\dot{v}_3 &= k_3 h_3(z_3 - g_3 v_3) \\
\dot{z}_4 &= k_4(-c_4 z_4(z_4 - w_{41})(z_4 - w_{42}) - b_4 v_4 - d_4 v_4 z_4 + I_{VN_{Re}}) \\
\dot{v}_4 &= k_4 h_4(z_4 - g_4 v_4)
\end{aligned}
\tag{2.7.2}
$$

The recovery variables v_i correspond to the net trans-membrane potential of the muscle cells, while the state variables $z_i = (1, \ldots, 4)$ correspond to the net trans-membrane potential of the muscle cells. The parameters c_i represent the pulse amplitude, while $w_{i1} < w_{i2}$ for $(i = 1, \ldots, 4)$ represent the excitation threshold and excited state, respectively. The parameters b_i and g_i affect the rest state, while h_i governs the excitability and controls the crude activation and duration of action potential. Muscle cells, unlike pacemaker cells, do not exhibit self-oscillatory behavior; they must be activated by an electrical signal from a pacemaker to produce a single response. The variable I_m (the index m corresponds to AT_{De}, AT_{Re}, VN_{De}, and VN_{Re}) in equation (2.7.2) denotes the amount of the stimulation current that couples the SA and HP pacemakers to the atrial (AT) and ventricular (VN) muscles, respectively; De and Re stand for depolarization and re-polarization. Finally, a linear combination of the electrical impulses from the AT and VN muscles yields the synthetic ECG waveform:

$$
ECG = z_0 + z_1 + z_2 + z_3 + z_4 \tag{2.7.3}
$$

The z_0 parameter determines the baseline of the ECG signal since the T_a wave is opposite the P wave, and the value of z_2 has a negative sign. The primary goal is to create a model that can accurately mimic the ECG of a healthy heart as well as that of VF, which is caused by several, short-lived, re-entrant electrical waves in the ventricles [21]. Therefore, authors regarded the mother rotor and/or numerous wavelets as a combined trigger source, represented by an EP, that stimulates the AT and VN muscles in their study. The extended model has a conceptual framework which is shown in figure (2.7).

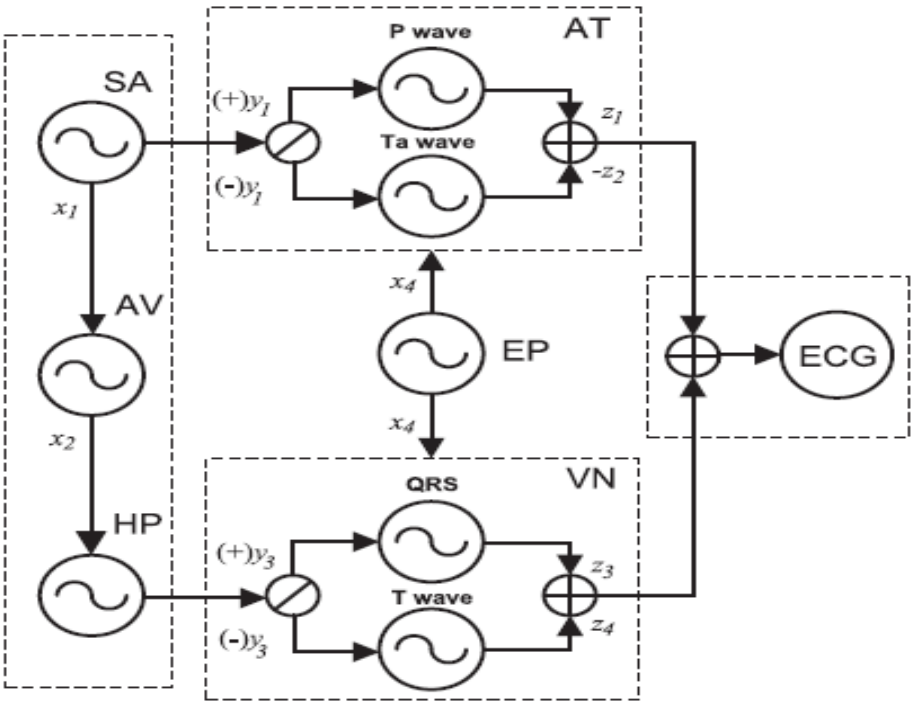

Figure 2.7: Schematic of the propose heterogeneous model [4]

The EP is a modified VDP oscillator, given by the following set of equations

$$\begin{aligned}\dot{x}_4 &= \beta_T y_4 \\ \dot{y}_4 &= \beta_T(-a_4 y_4(x_4-u_{41})(x_4-u_{42}) - f_4 x_4(x_4+d_4)(x_4+e_4)) + \beta_T A\sin\omega t,\end{aligned} \tag{2.7.4}$$

where β_T is the time scale adjustment coefficient in this case. The EP settings were chosen to produce chaotic oscillations as shown in figure (2.7) that are the primary cause of additional heart electrical excitation abnormalities, leading to cardiac arrest [25]. Furthermore, the EP is a stable mother rotor that is always maintained till the conclusion of the simulation duration, producing secondary excitation sources at a distance.
Extra variables are introduced in the system (2.7.2) to facilitate coupling of the EP with

the AT and VN muscles, which are given in equation (2.7.5):

$$
\begin{aligned}
\dot{z}_1 &= k_1(-c_1 z_1(z_1 - w_{11})(z_1 - w_{12}) - b_1 v_1 - d_1 v_1 z_1 + I_{AT_{De}} + k_{EP-AT}\, x_4) \\
\dot{v}_1 &= k_1 h_1(z_1 - g_1 v_1) \\
\dot{z}_2 &= k_2(-c_2 z_2(z_2 - w_{21})(z_2 - w_{22}) - b_2 v_2 - d_2 v_2 z_2 + I_{AT_{Re}} + k_{EP-AT}\, x_4) \\
\dot{v}_2 &= k_2 h_2(z_2 - g_2 v_2) \\
\dot{z}_3 &= k_3(-c_3 z_3(z_3 - w_{31})(z_3 - w_{32}) - b_3 v_3 - d_3 v_3 z_3 + I_{VN_{De}} + k_{EP-k_{EP-VN}}\, x_4) \\
\dot{v}_3 &= k_3 h_3(z_3 - g_3 v_3) \\
\dot{z}_4 &= k_4(-c_4 z_4(z_4 - w_{41})(z_4 - w_{42}) - b_4 v_4 - d_4 v_4 z_4 + I_{VN_{Re}} + k_{EP-VN}\, x_4) \\
\dot{v}_4 &= k_4 h_4(z_4 - g_4 v_4)
\end{aligned}
\tag{2.7.5}
$$

where k_{EP-AT} and k_{EP-VN} are the EP coupling constants. In what follows, only a ventricular stimulus will be considered, thus $k_{EP-AT} = 0$ and the corresponding coupling constant k_{EP-VN} will play the role of the control parameter.

Therefore, the coupling parameter k_{EP-VN} plays an important role in the dynamics

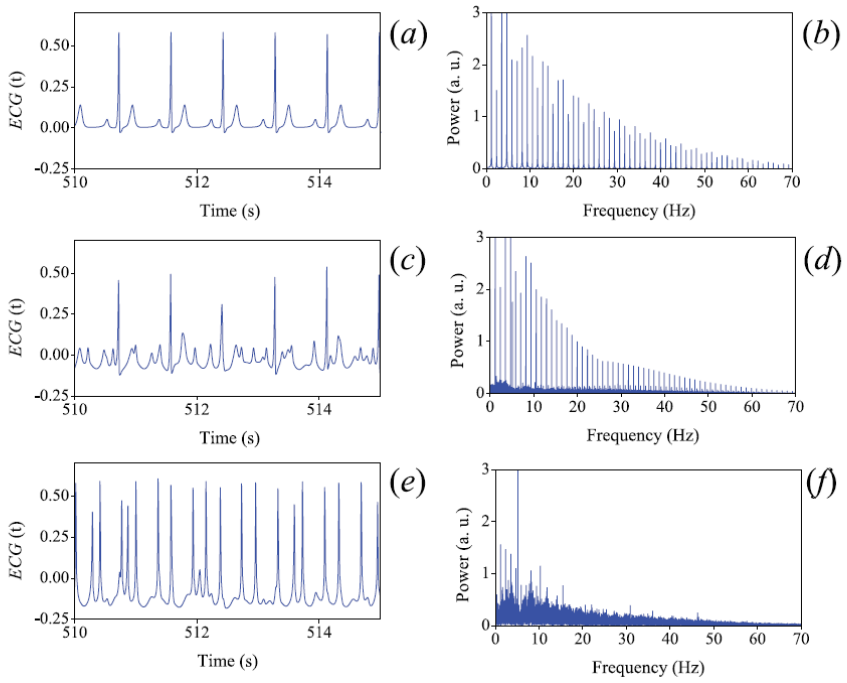

Figure 2.8: Time series (left column) and their corresponding frequencies (right column) for three distinct control parameter values k_{EP-VN}. (a) and (b) correspond to normal condition ($k_{EP-VN} = 0.0$), (c) and (d) to a quasi-periodic oscillation ($k_{EP-VN} = 0.001$), and (e) and (f) to VF ($k_{EP-VN} = 0.009$) [5]

of the ECG of the heart. So when $k_{EP-VN} = 0$, it corresponds to the original model of equation (2.7.2), and the ECG displays is in the normal rhythm or the sinus rhythm. Increasing the coupling parameter, the model follows a quasi-periodic route to chaos and exhibits VF which is shown in figure (2.8).

Chapter 3

Identification and Analysis of Bifurcations

3.1 Mapping Reaction-diffusion Equation to Electrical Activity of the Heart

The reaction-diffusion equation is used to model a variety of biologically important real-life phenomena. By assuming the mass conservation of the two morphogens, expanding through the Taylor series, and limiting the degree of the equation to three, this model can be reduced to two first-order partial differential equations (PDE). The Barrio-Varea-Aragon-Maini (BVAM) model [26] is the name of this model. Turing patterns, traveling waves, temporal oscillations, and chaotic behavior are all examples of real-world applications of this model [27]. These equations are given in (3.1.1),

$$\begin{aligned} \frac{\partial u}{\partial t} &= D\nabla^2 u + \eta(u + av - Cuv - uv^2) \\ \frac{\partial v}{\partial t} &= \nabla^2 v + \eta(bv + Hu + Cuv + uv^2) \end{aligned} \tag{3.1.1}$$

consist of two PDEs can be interpreted as some chemical substances, morphogens, or any other measurable quantity morphogens or current. The state variables $u = u(x,t)$ and $v = v(x,t)$ are dependent upon position x and time t. The parameters of the system are H, η, D, C, and b. For the concerned system, the values of some of the parameters are fixed. These parameters value are $\eta = 1, a = -1$, and $b = -3$. This can be discretized at three distinct nodes which are mainly responsible for actuating the heart. These nodes physically are known to be SA Node, AV Node, and Purkinje complex. The electrical

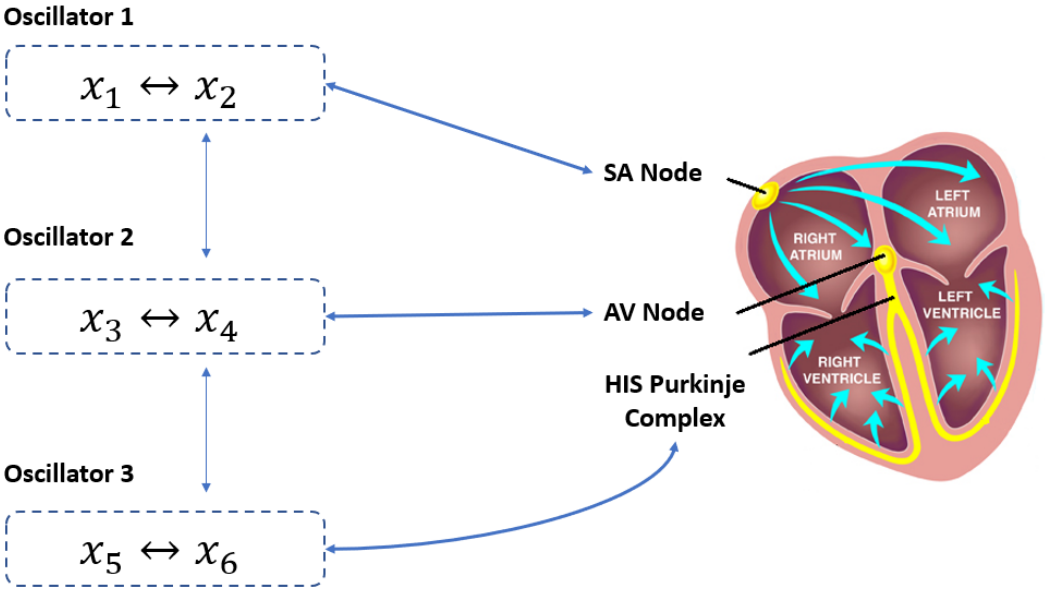

Figure 3.1: SA Node, AV Node, and HIS-Purkinje complex and three oscillators of the BVAM model $x_1 - x_6$ given in equation (3.1.5)

system of the heart as described in the previous sections is mainly represented by these three nodes,

$$\begin{aligned} \frac{\partial u}{\partial x}|_{FD} &= \frac{u_i - u_{i-1}}{\Delta x} \\ \frac{\partial v}{\partial x}|_{FD} &= \frac{v_i - v_{i-1}}{\Delta x}, \end{aligned} \tag{3.1.2}$$

$$\begin{aligned} \frac{\partial u}{\partial x}|_{BD} &= \frac{u_i - u_{i-1}}{\Delta x} \\ \frac{\partial v}{\partial x}|_{BD} &= \frac{v_i - v_{i-1}}{\Delta x}. \end{aligned} \tag{3.1.3}$$

The PDE (3.1.1) can be discretized to form a set of ODEs and for this purpose, forward and backward differentiation is used. The mathematical expression of forward and backward differential equations are shown in equations (3.1.2) and (3.1.3). The PDE (3.1.1) is discretized at three nodes with two additional nodes as the boundary conditions. Using the relationships provided in equations (3.1.2) and (3.1.3) on each node of figure (3.2) and using Neumann boundary conditions provided in equation (3.1.4), one arrives at equation (3.1.5),

$$\begin{aligned} \frac{\partial u}{\partial x} &= \frac{u_i - u_0}{\Delta x} = 0 \\ \frac{\partial v}{\partial x} &= \frac{v_i - v_0}{\Delta x} = 0, \end{aligned} \tag{3.1.4}$$

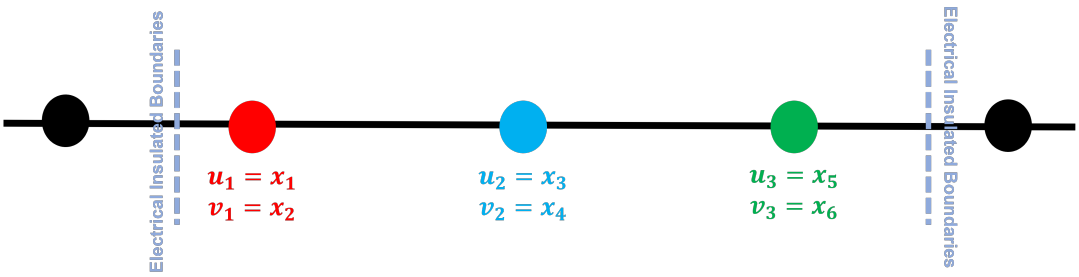

Figure 3.2: Discretization of (3.1.1) at three different nodes SA node, AV node, and HIS-Purkinje complex

$$\begin{aligned}
\dot{x}_1 &= x_1 - x_2 - Cx_1x_2 - x_1{x_2}^2 \\
\dot{x}_2 &= Hx_1 - 3x_2 + Cx_1x_2 + x_1{x_2}^2 + \beta(x_4 - x_2) \\
\dot{x}_3 &= x_3 - x_4 - Cx_3x_4 - x_3{x_4}^2 \\
\dot{x}_4 &= Hx_3 - 3x_4 + Cx_3x_4 + x_3{x_4}^2 + \beta(x_6 - 2x_4 + x_2) \\
\dot{x}_5 &= x_5 - x_6 - Cx_5x_6 - x_5{x_6}^2 \\
\dot{x}_6 &= Hx_5 - 3x_6 + Cx_5x_6 + x_5{x_6}^2 + \beta(x_4 - x_6).
\end{aligned} \tag{3.1.5}$$

The Neumann boundary condition states that there should be no flux passage across the boundary. This essentially implies that the value of the state at the boundary will be equal to the state right beside the boundary, if the value of state outside the boundary is taken to be x_0 it means, implying equation (3.1.4) that $x_1 = x_{10}$ and $x_2 = x_{20}$. Similarly at the other side of the boundary $x_5 = x_{10}$ and $x_6 = x_{20}$. These kinds of boundary conditions imply that now current is escaping the boundaries and helps to reduce the complexity of the under-considered system. Using these boundary conditions further dictates that $x_1 = x_5$ and $x_2 = x_6$. It means that the SA node and HIS-Purkinje complex are mathematically symmetrical. Therefore the order of the system is reduced to in total four first-order nonlinear ODE

$$\begin{aligned}
\dot{x}_1 &= x_1 - x_2 - Cx_1x_2 - x_1{x_2}^2 \\
\dot{x}_2 &= Hx_1 - 3x_2 + Cx_1x_2 + x_1{x_2}^2 + \beta(x_4 - x_2) \\
\dot{x}_3 &= x_3 - x_4 - Cx_3x_4 - x_3{x_4}^2 \\
\dot{x}_4 &= Hx_3 - 3x_4 + Cx_3x_4 + x_3{x_4}^2 + 2\beta(x_2 - x_4).
\end{aligned} \tag{3.1.6}$$

3.2 Nonlinear Analysis of Fixed Points (FP)

When the value of the control parameter (H) is varied, the mathematical model under consideration (3.1.6) exhibits various types of solutions. FP solutions for ($H > 8.77$), stable limit cycles, period two oscillations, quasi-periodic attractors, and chaotic solutions are among the types of solutions. A trajectory initiated from any point in the phase plate, for example, will eventually lead to a single point attractor at ($H = 9$). This FP attractor can be discovered by considering the condition $\dot{\mathbf{x}} = \mathbf{0}$ at which this attractor will be found. A set of algebraic equations with unknowns is created by this condition. Given equation (3.2.1) can be written compactly as equation (3.1.6).

$$\dot{\mathbf{x}} = \mathbf{F}(\mathbf{x}, H) \tag{3.2.1}$$

The condition for locating FP attractors is given in the equation, which, when applied to the original system of equations (3.1.6), yields four nonlinear algebraic equations with four unknowns.

$$\mathbf{F}(\mathbf{x}, H) = \mathbf{0} \tag{3.2.2}$$

$$\begin{aligned} x_1 - x_2 - Cx_1x_2 - x_1{x_2}^2 &= 0 \\ Hx_1 - 3x_2 + Cx_1x_2 + x_1{x_2}^2 + \beta(x_4 - x_2) &= 0 \\ x_3 - x_4 - Cx_3x_4 - x_3{x_4}^2 &= 0 \\ Hx_3 - 3x_4 + Cx_3x_4 + x_3{x_4}^2 + 2\beta(x_2 - x_4) &= 0 \end{aligned} \tag{3.2.3}$$

To solve the equations in equation (3.2.3), a nonlinear iterative scheme can be used. There are eight possible solutions, five of which are complex numbers. Since it is known that FP must be real for a physical system, the real FP is the only one that remains. Table (3.1) contains the three FPs. The set of FP is the trivial solution, as shown in

FP	x_1	x_2	x_3	x_4
FP 1	0	0	0	0
FP 2	−1.1975	−1.29	1.5284	0.4136
FP 3	0.8963	0.3546	−2.1215	−1.5315

Table 3.1: FP of BVAM model at $H \approx 9$

table (3.1), while the other two fixed pints are also mentioned. Any trajectory that

begins in the phase plane will now be drawn to one of these FPs. The initial conditions determine which of these FPs will be the final destination of a phase plane trajectory. It is necessary to conduct a stability analysis of these FPs before proceeding. This stability analysis holds only in the immediate vicinity of these FPs. Therefore, the system of equations given in equation (3.1.6) must be linearized. The linear form of a system of equations is represented by the Jacobian J of a system. When a FP is inserted in the Jacobian J, the dynamics of the system are reduced to a local region of a FP. The Jacobian can be expressed as a form of equation (3.2.4),

$$J = \begin{bmatrix} \frac{\partial F_1}{\partial x_1} & \frac{\partial F_1}{\partial x_2} & \frac{\partial F_1}{\partial x_3} & \frac{\partial F_1}{\partial x_4} \\ \frac{\partial F_2}{\partial x_1} & \frac{\partial F_2}{\partial x_2} & \frac{\partial F_2}{\partial x_3} & \frac{\partial F_2}{\partial x_4} \\ \frac{\partial F_3}{\partial x_1} & \frac{\partial F_3}{\partial x_2} & \frac{\partial F_3}{\partial x_3} & \frac{\partial F_3}{\partial x_4} \\ \frac{\partial F_4}{\partial x_1} & \frac{\partial F_4}{\partial x_2} & \frac{\partial F_4}{\partial x_3} & \frac{\partial F_4}{\partial x_4} \end{bmatrix} \tag{3.2.4}$$

while the eigenvalues of a Jacobian matrix are significant because they reveal information about the stability of the system. The eigenvalues of a linear system are usually expressed in exponential terms. The eigenvalues are frequently complex numbers, with the real part representing rise and decay and the imaginary part frequently representing frequency. Therefore, the eigenvalues with a positive real part (if they are complex) indicate that the response of the system will eventually rise to infinity from the FP. The eigenvalues with a negative real part, on the other hand, represent a system response approaching a FP. When all of the eigenvalues corresponding to a FP are negative, the FP is said to be stable. The corresponding FP is unstable if any of the eigenvalues are positive. Although, the negative eigenvalues in this case attempt to bring the trajectory to a FP along the corresponding eigenvector, which is referred to as manifold in a global region, the impact of just one positive eigenvalue is sufficient to cause any trajectory initiated at any point other than the stable manifolds to deviate from that FP in the phase plane. The eigenvalues of the Jacobian matrix for FP are shown in table (3.2),

FP	Eigenvalues of Jacobian
FP 1	$-14.42, 0.42, -1 \pm 2.24\iota$
FP 2	$-8.83, -2.48, -0.27 \pm 5.38\iota$
FP 3	$-7.3, -3.7, -0.04 \pm 5.8\iota$

Table 3.2: The eigenvalues of the Jacobian matrix of BVAM model for the FP at $H \approx 9$

which indicates the system's stability. The trivial FP is unstable, as shown in table (3.2). Therefore, it is unlikely that any trajectory will lead to it $t \to \infty$.
The FP in table (3.1) changes continuously as the value of control parameter H changes, and the state of stability can change at a certain value of H. A bifurcation is responsible for this change of behavior. When one of these eigenvalues has zero real part, the bifurcation of these FP can be seen. Since the effects of the positive and negative real parts of the eigenvalues have been discussed, the zero real part of an eigenvalue shows no rise or decay but a constant amplitude of oscillations, indicating that the system is marginally stable.

3.3 Hopf Bifurcation

Hopf bifurcation is a term used to describe the transition from a FP solution to a periodic solution. The system's stable FP becomes unstable in a supercritical Hopf bifurcation. According to study [6], three conditions must be met for Hopf bifurcation to occur at the critical value of the control parameter.

1. $\mathbf{F}(\mathbf{x_0}, H_c) = \mathbf{0}$.
2. The Jacobian system of equation (3.1.6) has at least one pair of purely imaginary values while all other eigenvalues have the non-zero real part at that particular FP $\mathbf{x_0}$ and control parameter value H_c.
3. At $H = H_c$, let the analytical continuation of purely imaginary value be $\lambda \pm \iota\omega$ then $\frac{d\lambda}{dH} \neq 0$. This is called the transversality condition.

FP is indicated by the first condition, while non-hyperbolic FP is indicated by the second condition. When the value of a control parameter is changed, the transversality condition implies an exchange of stability. Table (3.3) shows the FP and corresponding

H	FPs	Eigenvalues of Jacobian
8.77	0.92, 0.36, −2.18, −1.54	$-7.36, -3.86, \pm 5.82\iota$
8.50	$0.96, 0.36, -2.27, -1.55$	$-6.9, -4.1, 0.05 \pm 5.85\iota$

Table 3.3: FP and the eigenvalues at different values of H for FP 3

the eigenvalues for FP 3 from table (3.1) at $H = 8.77$ and $H = 8.50$. FP and the

eigenvalues for FP 3 at $H = 9$ are already listed in tables (3.1) and (3.2), respectively. The eigenvalue with zero real part indicates that the FP 3 from table (3.1), loses stability at $H = 8.77$, as indicated by the eigenvalue. Since the real part of the specific eigenvalue becomes positive, the transversality condition is satisfied. The frequency that is added at this bifurcation point is the pure imaginary part of the eigenvalue at the critical control parameter value $H = H_c = 8.77$ i.e. $\omega = 5.82$. Therefore, the FP at H_c lost its stability, and the process continued while a stable branch of a periodic solution emerged from the bifurcation point. The supercritical Hopf bifurcation is the name given to this particular bifurcation.

At $H = 7.97$, the same thing happens with FP 2 from table (3.1). The critical value of the control parameter causes a stable branch of FP to lose its stability and become unstable, resulting in the emergence of a stable periodic solution. This is demonstrated by table (3.4) as well as analysis of tables (3.1) and (3.2). There are three unstable FP

H	FPs	Eigenvalues of Jacobian
7.97	-1.41, -1.37, 1.8, 0.43	$-7.5, -3.35, \pm 5.56\iota$
7.95	$-1.42, -1.37, 1.8, 0.43$	$-7.46, -3.38, 0.006 \pm 5.56\iota$

Table 3.4: FP and eigenvalues at different values of the control parameter for FP 2

(all three emerged from table (3.1)) and two stable periodic solutions, the branches that emerged from the Hopf bifurcation point for the corresponding FP, at this point for the local region of $H < 7.97$.

3.4 Period Two Solution

For a given range of control parameter values, the BVAM model appears to have a two-period solution. On-time series data, a two-period solution can be identified by two peaks. There are two dots visible on a Poincare section of a period two solution, compared to one dot for a periodic solution. The Poincare section is frequently used to visualize and detect period-doubling bifurcation in period two solutions. The Poincare section is a plane used to find the intersection of a phase plane trajectory with the Poincare section. After a time period, the Poincare section can also be used to find the intersection with time serious data T. Therefore, a single period solution appears as

a single dot on the Poincare section, whereas at the period-doubling bifurcation point, where the period is abruptly doubled, two dots appear on the Poincare section as an indicator of period-doubling bifurcation and represent a period two solution.

The Floquet multipliers must be found to detect a period-doubling bifurcation analytically. These Floquet multipliers provide crucial information about a periodic solution's bifurcation. The eigenvalues of a monodromy matrix are called Floquet multipliers, and they are often complex numbers. According to literature [6], one of the Floquet multipliers associated with any periodic solution is always unity, indicating that the solution has a periodic behavior. All other Floquet multipliers in a stable periodic solution lie within the complex plane's unit circle. If any of the Floquet multipliers are outside the unit circle for any solution, it indicates that the solution is unstable. If any of the Floquet multipliers other than unity are found at the circumference of the unit circle, the corresponding system has become non-hyperbolic, and some sort of bifurcation is possible. The type of bifurcation that occurs is determined by the route taken by the Floquet multipliers as they leave the unit circle. It was pointed out that if a Floquet multiplier leaves the unit circle through -1, it indicates a possible period-doubling bifurcation [6]. The shooting method is used to create periodic solutions and to find the Floquet multipliers that go along with them. A periodic solution in the phase plane appears as a closed trajectory in the phase plane and can be found in the exact initial conditions of these periodic solutions are known, such that no transients appear in the first part of the time series data. Because the system of equations is numerically simulated only until the time period T in the shooting method, it is also necessary to find the time period. The algorithm is first initialized with a set of arbitrary initial conditions $\boldsymbol{\eta_0}$ and a time period T_0 in the shooting method. The algorithm then performs several iterations to determine the appropriate initial conditions $\boldsymbol{\eta}$ and time period T for the periodic solution to appear.

The periodic solution is not formed after the first iteration of the shooting method, where the system of equations (3.1.6) is integrated up until the time period (T_0), because the arbitrarily chosen initial conditions $\boldsymbol{\eta_0}$ and the time period T_0 are not correct, and the only way forward is to move towards the right set of initial conditions $\boldsymbol{\eta}$ and time period T. It is desired to reduce $\boldsymbol{\delta\eta_0} = \boldsymbol{\eta} - \boldsymbol{\eta_0}$ and $\delta T = T - T_0$ to satisfy equation (3.4.1). The periodic solution is not formed after the first iteration of the shooting method, where the system of equations (3.1.6) is integrated up until the time period T_0), because the

arbitrarily chosen initial conditions $\boldsymbol{\eta_0}$ and the time period T_0 are not correct, and the only way forward is to move towards the right set of initial conditions $\boldsymbol{\eta}$ and time period T. It is desired to reduce $\boldsymbol{\delta\eta_0} = \boldsymbol{\eta} - \boldsymbol{\eta_0}$ and $\delta T = T - T_0$ to satisfy equation (3.4.1).

Equation (3.4.1) implies that the initial and final points of a trajectory in phase space are the same, implying that the solution obtained is periodic. The obtained equations are shown in equation (3.4.2), which can be expanded in the Taylor series by retaining only the linear terms. $\frac{\partial \mathbf{x}}{\partial \boldsymbol{\eta}}(T_0, \boldsymbol{\eta_0})$ and I are an $n \times n$ matrix where I is $n \times n$ matrices, with I being an identity matrix $\frac{\partial \boldsymbol{x}}{\partial T}(T_0, \boldsymbol{\eta_0}) = \mathbf{F}(T_0, \boldsymbol{\eta_0})$ is a $n \times 1$ vector.

$$\mathbf{x}(T_0 + \delta T, \boldsymbol{\eta_0} + \delta\boldsymbol{\eta}) - (\boldsymbol{\eta_0} + \delta\boldsymbol{\eta}) \approx \mathbf{0} \tag{3.4.1}$$

$$[\frac{\partial \mathbf{x}}{\partial \boldsymbol{\eta}}(T_0, \boldsymbol{\eta_0}) - I]_{n\times n}\delta\boldsymbol{\eta} + \frac{\partial \boldsymbol{x}}{\partial T}(T_0, \boldsymbol{\eta_0})\delta T = \boldsymbol{\eta_0} - \mathbf{x}(T_0, \boldsymbol{\eta_0}) \tag{3.4.2}$$

The four unknowns for $\frac{\partial \boldsymbol{x}}{\partial T} = \mathbf{F}(T_0, \boldsymbol{\eta_0})$ can be determined numerically using the integrating equation (3.1.6). The final values of the integration at $t = T_0$ will be the unknowns. The unknowns associated with $\frac{\partial \mathbf{x}}{\partial \boldsymbol{\eta}}$ can be determined by first calculating the time derivative, as shown in equation (3.4.3). Numerically integrating equation (3.4.3) yields the value of the 16 unknowns $\frac{\partial \mathbf{x}}{\partial \boldsymbol{\eta}}$ at $t = T_0$. Equation (3.4.5) is a $n \times n$ identity matrix that contains the initial conditions for equation (3.4.3).

$$\frac{\partial \dot{\boldsymbol{x}}}{\partial \boldsymbol{\eta}} = D_{\boldsymbol{x}}\boldsymbol{F}(\boldsymbol{x}; M)\frac{\partial \boldsymbol{x}}{\partial \boldsymbol{\eta}} \tag{3.4.3}$$

with the initial condition,

$$\frac{\partial x}{\partial \eta}(\mathbf{0}) = I \tag{3.4.4}$$

where $D_{\boldsymbol{x}}\boldsymbol{F}$ is the Jacobian matrix shown in equation (3.2.4) and $\frac{\partial \boldsymbol{x}}{\partial \boldsymbol{\eta}}$ is shown in equation (3.4.5)

$$\frac{\partial \boldsymbol{x}}{\partial \boldsymbol{\eta}} = \begin{bmatrix} \frac{\partial X_1}{\partial \eta_1} & \frac{\partial X_1}{\partial \eta_2} & \frac{\partial X_1}{\partial \eta_3} & \frac{\partial X_1}{\partial \eta_4} \\ \frac{\partial X_2}{\partial \eta_1} & \frac{\partial X_2}{\partial \eta_2} & \frac{\partial X_2}{\partial \eta_3} & \frac{\partial X_2}{\partial \eta_4} \\ \frac{\partial X_3}{\partial \eta_1} & \frac{\partial X_3}{\partial \eta_2} & \frac{\partial X_3}{\partial \eta_3} & \frac{\partial X_3}{\partial \eta_4} \\ \frac{\partial X_4}{\partial \eta_1} & \frac{\partial X_4}{\partial \eta_2} & \frac{\partial X_4}{\partial \eta_3} & \frac{\partial X_4}{\partial \eta_4} \end{bmatrix}. \tag{3.4.5}$$

There are 20 equations with 21 unknowns at this point. The system's time period is an additional unknown. The integration of all previous 20 equations can result in a set of initial conditions with a periodic solution if it is known.

The orthogonality condition can be used to meet the requirement of approximating the time period variable. The initial conditions must be in a direction perpendicular to the

trajectory flow in any phase plane, according to this equation. Overall, we can represent equation (3.4.6) for describing the shooting method

$$\begin{bmatrix} \frac{\partial \boldsymbol{x}}{\partial \boldsymbol{\eta}}(T_0, \boldsymbol{\eta_0}) - I & \boldsymbol{F}(\boldsymbol{\eta_0}; \boldsymbol{M}) \\ \boldsymbol{F}(\boldsymbol{\eta_0}; \boldsymbol{M}) & 0 \end{bmatrix} \begin{bmatrix} \delta\boldsymbol{\eta} \\ \delta T \end{bmatrix} = \begin{bmatrix} \boldsymbol{\eta_0} - \boldsymbol{x}(T_0, \boldsymbol{\eta_0}) \\ 0 \end{bmatrix}. \tag{3.4.6}$$

Iterating with the above equations until $||\delta\boldsymbol{\eta}|| < \epsilon_1$ and $\delta T < \epsilon_2$ are obtained, where ϵ_1 and ϵ_2 are small numbers, yields the required initial conditions and the time period of the system of equations given in equation (3.1.6). Monodromy matrix $\phi = \frac{\partial \boldsymbol{x}}{\partial \boldsymbol{\eta}}$ is produced as a by-product of the shooting method and is given in equation (3.4.5).

3.4.1 Period Doubling Bifurcation

A periodic solution, as well as the Floquet multipliers associated with it, can be obtained using the shooting method. The shooting method has the advantage of being able to identify the unstable periodic solution as well. As previously discussed, the Floquet multipliers provide crucial information about the stability of the solution and bifurcations. As discussed in the section where the Hopf bifurcation generated these two periodic solutions, there were two stable periodic solutions. As seen in table (3.1), one of the periodic solutions that originated from FP 3 of table (3.1), through the Hopf bifurcation at $H = 8.77$ undergoes period-doubling bifurcation at $H = 4.625$. The Floquet multipliers are all under the unit circle except one, for $H > 4.625$, and the periodic solution becomes non-hyperbolic at $H = 4.625$, and the result shows that the periodic solution becomes unstable after that, and it continues to be so for the later part where $H < 4.625$. Now, as shown in table (3.5), one of the Floquet multipliers -1 left the unit circle at $H = 4.625$ and thus at later values, it can be seen that it left the unit circle through the value -1, implying that a stable period two cycle has emerged from this point. Period doubling bifurcation occurs at this point $H = 4.625$.

The stable periodic solution, which originated through Hopf bifurcation at $H = 7.97$ from FP 2 in table (3.1), is the same. As can be seen from table (3.6), this period one cycle undergoes period-doubling bifurcation at $H = 4.565$. One of the Floquet multipliers, similar to the other branch, leaves a unit circle through -1 at $H = 4.565$, while the other stays at 1 at $H = 4.565$. The stable periodic solution becomes unstable, and a stable period two solution emerges $H \leq 4.565$ and remains stable for a time. Three unstable FP, two unstable periods one solution, and two stable periods two solutions

H	Floquet multipliers	Remarks
4.65	1 -0.91 -0.24 0	Periodic cycle
4.63	1 -0.99 -0.62 0	Periodic cycle
4.625	1 -1 -0.61 0	Non-hyperbolic point
4.62	1 -1.01 -0.61 0	Period doubled cycle
4.60	1 -1.04 -0.60 0	Period doubled cycle

Table 3.5: Floquet multipliers for first stable periodic solution

can be found near $H \leq 4.565$.

H	Floquet multipliers	Remarks
4.58	1 -0.93 -0.33 0	Periodic cycle
4.57	1 0.98 -0.32 0	Periodic cycle
4.565	1 -1 -0.32 0	Non-hyperbolic point
4.56	1 -1.01 -0.32 0	Period doubled cycle
4.55	1 -1.05 -0.32 0	Period doubled cycle

Table 3.6: Floquet multipliers for second stable periodic solution

Chapter 4

Analytical Solution Approximation

An analytical solution can be written in the form of an algebraic equation. This solution is displayed in terms of parameters and their relation with each other providing useful information to attain the required response from that specific system. Approximation of analytical is not straightforward for a nonlinear ODE. For linear equations usually, an analytical solution is accurate. However, in the case of nonlinear ODEs, the approximation can have some error. Nonetheless, an analytical solution serves its purpose by providing useful insight into the system.

The considered system of equation (3.1.6) consists of four first-order nonlinear ODEs with quadratic and cubic nonlinearities. By investigating numerically, it can be seen that the BVAM model has multiple solutions at each value of control parameter H. These solutions are stable as well as unstable. For example, as seen in the previous chapter from the table (3.1). At $H = 9$ there are three FPs. From there the stability analysis of FPs (refer to table (3.2), it is seen that the trivial FP are unstable while the nontrivial FPs are stable.

From the identification of the control parameter value where Hopf bifurcation occurs from the table (3.3) and table (3.4), the eigenvalues of the linearized system show the occurrence of a periodic solution along with other stable and unstable FPs and other periodic solution in case of Hopf bifurcation at $H = 7.97$. The case is similar for another control parameter H values. This brings a problem when trying to approximate an analytical solution. In doing simulation of the model given in equation (3.1.6) numerically,

the type of solution form depends upon the value of the control parameter as well as the value of initial conditions.

If the value of the control parameter is fixed $H = c$, even then there are multiple solutions as evidenced before. The type of solution formed at the end depends upon the initial condition. A trajectory in phase space is usually attracted to a stable solution near it.

4.1 Invariant Manifolds

An invariant subspace or manifold can be seen as a subspace with a set of initial conditions such that any solution initiated from these initial conditions remains in the same subspace. To understand the concept of manifolds, eigenvectors can play an important role. In fact eigenvectors are the subspace for a linearized system,

$$\begin{aligned} E^s &= span[\mathbf{p_1}, \mathbf{p_2}, \ldots, \mathbf{p_s}] \\ E^u &= span[\mathbf{p_{s+1}}, \mathbf{p_{s+2}}, \ldots, \mathbf{p_{s+u}}] \\ E^c &= span[\mathbf{p_{s+u+1}}, \mathbf{p_{s+u+2}}, \cdots, \mathbf{p_{s+u+c}}] \end{aligned} \tag{4.1.1}$$

and for a linear system of ODE, any trajectory follows a path given by eigenvectors with a pace given by an eigenvalue at the exponential ($e^{\lambda t}$). A system with positive eigenvalues diverges from a FP or periodic attractor while the negative eigenvalues converge towards an attractor. For a system described by equations (4.1.1), any solution initiated in the span of any eigenspace E^s, E^u or E^c, which is a subspace of a system, the solution will remain in that subspace of system.

Linear and nonlinear manifolds are shown in figure (4.1). In figure (4.1a) the linear manifolds or the subspaces are the eigenvectors of the linearized system. These eigenvectors or subspaces are only valid in the local region to a certain FP or another point of interest. As we move away from a FP, the shape of the manifold is curved. Therefore, the eigenvectors are not the ideal representation of a manifold in the global domain. One simple trick in numerically plotting the manifolds is to first calculate the eigenvectors of the linearized system. These eigenvectors correspond to the subspace and are valid only in the local region. Then take a point on the eigenvector very near to the FP and then simulate numerically with the initial conditions corresponding to the point

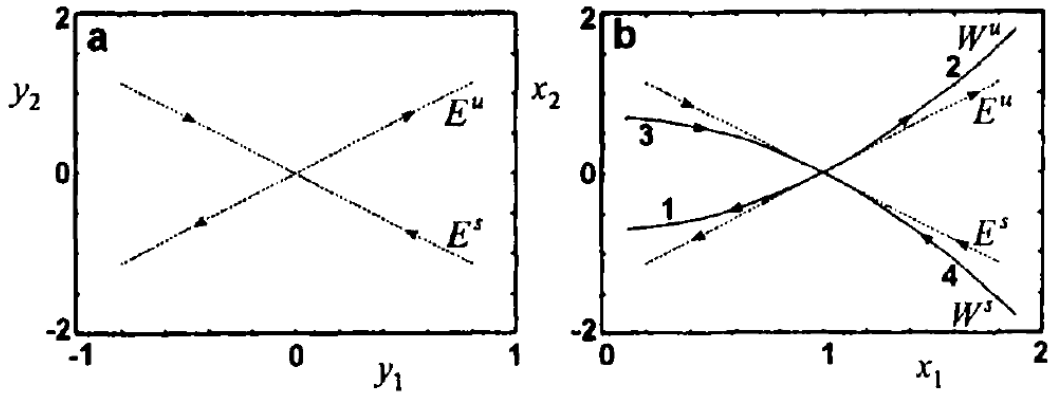

Figure 4.1: Manifolds of a system: picture (a) shows stable E^s subspace and unstable E^u subspace and (b) shows the corresponding nonlinear subspace or the manifolds [6]

chosen near the FP at the eigenvector which is a subspace. The numerical simulation should be done as $t \to \infty$ in case a subspace is a stable subspace E^s. The manifold form because of numerical simulation will be stable manifold W^s. This stable subspace E^s and stable manifold W^s are shown in figure (4.1b). The unstable manifold W^u can be plotted similarly from an unstable subspace E^u however, the numerical simulations are performed such that $t \to -\infty$ and this manifold is also shown in figure (4.1b).

Manifolds of a solution play an important role in forming the overall solutions. Numerically a solution follows the path of an attractor or a repeller near it. This attractor is defined by the manifolds of a solution. Therefore, if someone wants to find a periodic solution to a system, he should focus on the center manifold. This pretty much does answer our original problem about which solution we are trying to approximate analytically.

The next question which arises is that can we find those manifolds of a system and its answer is yes. If someone knows the FPs from where a manifold is passing through, then one can make transformations to that manifold. The equations of these manifolds in the transformed version are ODEs. These manifolds equations represent distinct manifolds such as stable, unstable, and center manifolds. These manifolds are usually coupled. In many cases, it is desired to uncouple these manifolds so that the analysis is performed on the required manifolds and the required solution is attained without going into the details of other manifolds. In such a case, the other manifolds are approximated in terms of a polynomial expression of those manifold variables.

4.2 Center Manifold Reduction

Since equations (3.1.6) have multiple solutions even at a single value of control parameter, focus on one specific solution can be made by finding the manifolds of that solution. Since we are trying to find out the periodic solution of the system (3.1.6), the associated manifold is the center manifold. After transforming equations (3.1.6) to its manifolds, which are coupled. Analysis of the center manifold reveals the specific periodic behavior. However, to further ease the analysis, it is recommended that the analysis is focused on the center manifold only, which means that the other manifold variables e.g., stable and unstable should be decoupled from the center manifold equations.

4.2.1 Translation of Origin

First, it is needed to concentrate on the specific periodic solution. Considering FP 2 or FP 3 from the table (3.1). These points according to the table (3.3) and table (3.4) respectively, undergo a Hopf bifurcation as discussed in chapter (3). So keeping the value of the control parameter near this critical value i.e., $H = 8.77$ or $H = 7.97$ a periodic solution is being formed. Let us focus our attention at $H = 7.97$. At the exact value of the control parameter, two stable manifolds are corresponding to a negative eigenvalue of the Jacobian matrix which is the subset of the initial condition which can bring a trajectory in phase space right toward that FP. However, there forms a new manifold corresponding to the pure imaginary eigenvalue of the Jacobian matrix. These eigenvalues of the Jacobian matrix can be seen in the table (3.3).

To begin with, it is needed to concentrate on the FP undergoing Hopf bifurcation so that the center manifold can be determined. This can be accomplished by using the relationship provided in equation (4.2.1). The FP 2 ($\mathbf{x_0}$) are derived for $H = 7.97$ and are given in table (3.4). The variable $\mathbf{y}$ is the disturbances to the FP $\mathbf{x_0}$

$$\mathbf{x} = \mathbf{x_0} + \mathbf{y}. \tag{4.2.1}$$

Applying the transformation of equation (4.2.1) to the set of equations (3.1.6), resulting in an equation whose origin is at the corresponding FP $\mathbf{x_0}$. After applying this transformation, equation (3.1.6) assumes the form given in equation (4.2.2). Here in equation (4.2.2), A is the Jacobian matrix of equation (3.1.6), $\mathbf{F_2}(\mathbf{y})$ represents the quadratic

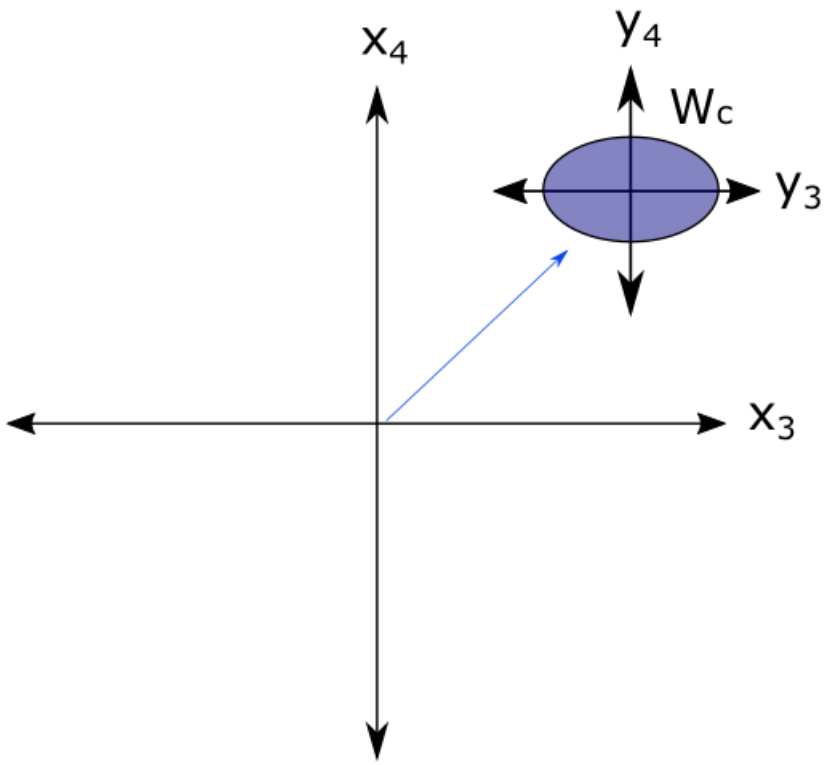

Figure 4.2: Origin translation from $\mathbf{x}$ to a new axis corresponding to $\mathbf{y}$ and W_c corresponds to center manifold

nonlinear terms involving the variable $\mathbf{y}$ and $\mathbf{F_3}(\mathbf{y})$ represent the cubic nonlinear terms in terms of variable $\mathbf{y}$

$$\dot{\mathbf{y}} = A\mathbf{y} + \sigma\mathbf{y} + \mathbf{F_2}(\mathbf{y}) + \mathbf{F_3}(\mathbf{y}) + O(||\mathbf{y}||^4). \tag{4.2.2}$$

This equation (4.2.2) in matrix form with coefficient values is shown by equation (4.2.3). Here the matrix A, control parameter terms, and quadratic and cubic nonlinear terms can be seen. The disturbance variable $\mathbf{y}$ has the same dimensions as of original variable

$\mathbf{x}$, which is 4×1

$$\dot{\mathbf{y}} = \begin{bmatrix} 0.969961 & -2.97135 & 0 & 0 \\ 8.0092 & -5.02865 & 0 & 4 \\ 0 & 0 & 0.238418 & -4.96362 \\ 0 & 8 & 8.73246 & -7.03638 \end{bmatrix} \cdot \begin{bmatrix} y_1 \\ y_2 \\ y_3 \\ y_4 \end{bmatrix} + \begin{bmatrix} 0 \\ -1.41438 + y_1 \\ 0 \\ 1.7963 + y_3 \end{bmatrix} \sigma + \begin{bmatrix} 1.39y_1y_2 + 1.41{y_2}^2 - y_1{y_2}^2 \\ -1.39y_1y_2 - 1.41{y_2}^2 + y_1{y_2}^2 \\ -2.21y_3y_4 - 1.80{y_4}^2 - y_3{y_4}^2 \\ 2.21y_3y_4 + 1.80{y_4}^2 + y_3{y_4}^2 \end{bmatrix}. \tag{4.2.3}$$

4.2.2 Transformation to get the Manifold Equations

For a solution at the control parameter value of $H = 7.97$ the FPs experiencing Hopf bifurcation along with the eigenvalues of the linearized system are given in the table (3.3). These eigenvalues show that there should be two stable manifolds corresponding to the negative real eigenvalues and a center manifold corresponding to the pure imaginary complex conjugate eigenvalues. There should be two manifolds corresponding to eigenvalues ± 5.82 of the linearized system. In the linearized system, the eigenvectors represent the linear manifolds so a transformation (4.2.4) is needed to transform the system to a linear manifold coordinate system. The matrix P in equation (4.2.4) is the matrix of eigenvectors for the linearized system of equation for equation (3.1.6),

$$\mathbf{y} = P\mathbf{v} \tag{4.2.4}$$

and after applying the transformation of equation (4.2.4) and multiplying both sides of equation with P^{-1} so that the form of equation involving the state variable $\mathbf{y}$ can be converted to $\mathbf{v}$. A general equation representation of the equation is shown in equation (4.2.5). Here the matrix J is the diagonal matrix while $\mathbf{F_2}(\mathbf{v})$ represents the quadratic nonlinear terms involving the variable $\mathbf{v}$ and $\mathbf{F_3}(\mathbf{v})$ represent the cubic nonlinear terms in terms of variable $\mathbf{v}$,

$$\dot{\mathbf{v}} = J\mathbf{v} + P^{-1}\mathbf{F_2}(P\mathbf{v}) + P^{-1}\mathbf{F_3}(P\mathbf{v}) + O(||\mathbf{v}||^4) \tag{4.2.5}$$

the diagonal matrix which essentially means that different manifolds, stable and center in our case are decoupled linearly. Although the manifolds are coupled non-linearly. An expanded form of equation (4.2.5) is given in equation (4.2.6). Linear decoupling and

nonlinear coupling can be seen more clearly in equation (4.2.6). The former equations are the general representation after transformation (4.2.4) has been applied on equation (4.2.3) and note that in our case there is no unstable manifold concerning the variable $\mathbf{v_u}$. Therefore the form we are dealing with looks closer to equation (4.2.7). This general representation is given here instead of writing the full equation since the original equation representing the transformation (4.2.7) is lengthy and is given in chapter (7) containing appendix.

$$\begin{bmatrix} \dot{\mathbf{v_c}} \\ \dot{\mathbf{v_s}} \\ \dot{\mathbf{v_u}} \end{bmatrix} = \begin{bmatrix} J_c & 0 & 0 \\ 0 & J_s & 0 \\ 0 & 0 & J_u \end{bmatrix} \begin{bmatrix} \mathbf{v_c} \\ \mathbf{v_s} \\ \mathbf{v_u} \end{bmatrix} + \begin{bmatrix} \mathbf{G_2}(\mathbf{v_c}, \mathbf{v_s}, \mathbf{v_u}) + \mathbf{G_3}(\mathbf{v_c}, \mathbf{v_s}, \mathbf{v_u}) \\ \mathbf{H_2}(\mathbf{v_c}, \mathbf{v_s}, \mathbf{v_u}) + \mathbf{H_3}(\mathbf{v_c}, \mathbf{v_s}, \mathbf{v_u}) \\ \mathbf{K_2}(\mathbf{v_c}, \mathbf{v_s}) + \mathbf{K_3}(\mathbf{v_c}, \mathbf{v_s}, \mathbf{v_u}) \end{bmatrix} + \sigma \begin{bmatrix} \mathbf{G_4}(\mathbf{v_c}, \mathbf{v_s}, \mathbf{v_u}) \\ \mathbf{H_4}(\mathbf{v_c}, \mathbf{v_s}, \mathbf{v_u}) \\ \mathbf{K_4}(\mathbf{v_c}, \mathbf{v_s}, \mathbf{v_u}) \end{bmatrix} \tag{4.2.6}$$

$$\begin{bmatrix} \dot{\mathbf{v_c}} \\ \dot{\mathbf{v_s}} \end{bmatrix} = \begin{bmatrix} J_c & 0 \\ 0 & J_s \end{bmatrix} \begin{bmatrix} \mathbf{v_c} \\ \mathbf{v_s} \end{bmatrix} + \begin{bmatrix} \mathbf{G_2}(\mathbf{v_c}, \mathbf{v_s}) + \mathbf{G_3}(\mathbf{v_c}, \mathbf{v_s}) \\ \mathbf{H_2}(\mathbf{v_c}, \mathbf{v_s}) + \mathbf{H_3}(\mathbf{v_c}, \mathbf{v_s}) \end{bmatrix} + \sigma \begin{bmatrix} \mathbf{G_4}(\mathbf{v_c}, \mathbf{v_s}) \\ \mathbf{H_4}(\mathbf{v_c}, \mathbf{v_s}) \end{bmatrix}. \tag{4.2.7}$$

For equation (4.2.7), J_c is the diagonal matrix representing the pure imaginary eigenvalues at its main diagonal entries, J_s s the diagonal matrix representing the real negative eigenvalues at its main diagonal entries, $\mathbf{G_2}(\mathbf{v_c}, \mathbf{v_s})$ is the function representing the quadratic nonlinear terms while $\mathbf{G_3}(\mathbf{v_c}, \mathbf{v_s})$ is representing the cubic nonlinear terms with the variable of course given as $\mathbf{v_c}, \mathbf{v_s}$. Now as can be interpreted with the eigenvalues at the diagonal entries, the equation in terms of state variables $\mathbf{v_c}$ is the equation of center manifold, and the equation concerning the variable $\mathbf{v_s}$ is the equation of stable manifold.

4.2.3 Decoupling Center Manifold from Stable Manifold

Transformation of the manifolds was done to focus on the specific type of solution. Now the transformed equation (4.2.7) containing the center and stable manifold is nonlinearly coupled. It will be helpful if we can somehow ignore the not required manifolds. If the stable manifolds from equation (4.2.7), can somehow be approximated in terms of center manifold variables, then the substitution of stable manifold variables in the center manifold equation eventually decouples the center manifold equation.

In the current analysis the manifold variables $\mathbf{v} = [v_1,\ v_2,\ v_3,\ v_4]^T$ contain the center manifold variables v_2, v_3 and stable manifold variables v_1, v_4. Therefore, to decouple the two center manifold equations from the two stable manifold equations, the center manifold is approximated in terms of stable manifold variables. The approximation

is done using polynomial series such as given in equation (4.2.8). There are certain properties for manifolds such that representing manifold in terms of a series such as given in equation (4.2.8) is subjected to certain conditions. These conditions are listed in equation (4.2.9), (4.2.10) and (4.2.11)

$$\begin{aligned} v_1 &= h_1(v_2, v_3, \sigma) = a_4\sigma + c_1 + c_2 v_2 + c_3 v_3 + a_1 {v_2}^2 + a_2 v_2 v_3 + a_3 {v_3}^2 + \dots \\ v_4 &= h_2(v_2, v_3, \sigma) = b_4\sigma + d_1 + d_2 v_2 + d_4 v_3 + b_1 {v_2}^2 + b_2 v_2 v_3 + b_3 {v_3}^2 + \dots . \end{aligned} \tag{4.2.8}$$

The manifold polynomial expressions (4.2.8) is subjected to conditions (4.2.9), (4.2.10) and (4.2.11) reduces some of the terms related to (4.2.8). The first condition (4.2.9) illustrates that the stable manifold variable should be at the FP when the center manifold variables are zero i.e., both manifolds should coincide at the FP. The second condition enlisted (4.2.10) and (4.2.11) says that the manifolds should be perpendicular to each other when passing through a FP

$$h_1(0,0,0) = 0, \qquad h_2(0,0,0) = 0 \tag{4.2.9}$$

$$\frac{\partial h_1}{\partial v_2}(0,0,0) = 0, \qquad \frac{\partial h_1}{\partial v_3}(0,0,0) = 0 \tag{4.2.10}$$

$$\frac{\partial h_2}{\partial v_2}(0,0,0) = 0, \qquad \frac{\partial h_2}{\partial v_3}(0,0,0) = 0. \tag{4.2.11}$$

Applying the conditions (4.2.9), (4.2.10) and (4.2.11) on the polynomial approximations of the stable manifolds given in equation (4.2.8) reduces it to equations (4.2.12) which are the approximations to the stable manifolds in terms of polynomial series of center manifold variables. Although the coefficients in equation (4.2.12) are still unknown. These coefficients can be determined by using the stable manifold equations from equation (4.2.7). Inserting these approximations (4.2.12) into the stable manifold expression and using the center manifold equation makes two equations with only center manifold variables v_2, v_3. Comparing the coefficients of both sides gives a certain number of algebraic equations. Solving these equations for unknowns gives the value of coefficients. These values of coefficients are given in table (4.1),

$$\begin{aligned} v_1 &= h_1(v_2, v_3, \sigma) = a_4\sigma + a_1 {v_2}^2 + a_2 v_2 v_3 + a_3 {v_3}^2 + \dots \\ v_4 &= h_2(v_2, v_3, \sigma) = b_4\sigma + b_1 {v_2}^2 + b_2 v_2 v_3 + b_3 {v_3}^2 + \dots \end{aligned} \tag{4.2.12}$$

and with values of coefficients known for equation (4.2.12) as given in table (4.1), the stable manifolds are well approximated and are in terms of center manifold variables. Inserting these expressions (4.2.12) into the center manifold equation consisting of v_2, v_2

Parameters	Values	Parameters	Values
a_1	$-0.26+0.17\iota$	b_1	$-0.20-0.27\iota$
a_2	0.99	b_2	2.099
a_3	$-0.26-0.17\iota$	b_3	$-0.20+0.27\iota$
a_4	-0.72	b_4	1.02

Table 4.1: Parameters for polynomial

from equation (4.2.7) decouples the center manifold equation from the other manifold variables. These equations are given in the expression (4.2.13) and (4.2.14). The center manifold equations (4.2.13) and (4.2.14) represent the periodic nature of the system of equation (3.1.6) at the specific area work is focused in the phase space. This area is the local region to the FP $\mathbf{x_0}$ from the table (3.3). Similar can be done for the other FP as well. Although the nature of the solution is periodic the coordinate system is not the original space in which the solution is required. The origin is translated (equation (4.2.1)) and more importantly transformed (equation (4.2.4)). However, one can always transform back to the original coordinates with back transformation using the same expressions as were used for transformations, once the solution is known,

$$\begin{aligned}\dot{v}_2(t) =&\iota\omega v_2(t)+c_0\sigma+(c_{132}\sigma+c_{131})\,v_2(t)^3+(c_{122}\sigma+c_{121})\,v_2(t)^2+(c_{322}\sigma+c_{321})\,v_3(t)v_2(t)^2\\&+(c_{332}\sigma+c_{331})\,v_3(t)^2v_2(t)+c_{112}\sigma v_2(t)+(c_{312}\sigma+c_{311})\,v_3(t)v_2(t)+(c_{232}\sigma+c_{231})\,v_3(t)^3\\&+(c_{222}\sigma+c_{221})\,v_3(t)^2+c_{212}\sigma v_3(t) \qquad (4.2.13)\\ \dot{v}_3(t) =&-\iota\omega v_3(t)+d_0\sigma+(d_{232}\sigma+d_{231})\,v_2(t)^3+(d_{222}\sigma+d_{221})\,v_2(t)^2+(d_{332}\sigma+d_{331})\,v_3(t)v_2(t)^2\\&+(d_{322}\sigma+d_{321})\,v_3(t)^2v_2(t)+d_{212}\sigma v_2(t)+(d_{312}\sigma+d_{311})\,v_3(t)v_2(t)+(d_{132}\sigma+d_{131})\,v_3(t)^3\\&+(d_{122}\sigma+d_{121})\,v_3(t)^2+d_{112}\sigma v_3(t). \qquad (4.2.14)\end{aligned}$$

The ODEs are first-order and complex and these two equations are similar to the pure imaginary eigenvalues, they are complex conjugates of each other. The coefficients are known and are given in the appendix. Their general form is as given $c_a=\alpha_a+\beta_a\iota$ and $d_b=\alpha_b+\beta_b\iota$ where a and b are integers from 1 to 13, where σ indicates how much the control parameter value is far from the bifurcation point. The dynamics of the system are reduced from four ODEs to two of them and the approximate representation is close to the Hopf bifurcation point i.e., $H=7.97+\epsilon\sigma$.

4.3 Method of Multiple Scales

An ODE can be solved using any of the perturbation techniques suitable at the moment. In the present work, the method of multiple scales is applied to solve the coupled complex conjugate nonlinear equations. In this perturbation technique, the solution is expanded in the form of power series, and along with that time is divided into different fast-moving and slow-moving scales. The idea is to separate the dynamics along the fast and slow-moving time scales such that a solution to the system can be found.

The original time $T_0 = t$ corresponds to the second arm of the watch, whereas slow changing time $T_1 = \epsilon t$ corresponds to the minute arm of the watch, and even slower time $T_2 = \epsilon^2 t$ corresponds to the hour arm of the watch. Therefore $\mathbf{v}(t) = \mathbf{v}(t, \epsilon t, \epsilon^2 t \ldots)$ becomes the variables. Therefore, variable dependence shifts from actual time t to different fast and slow time scales $T_0, T_1, T_2, \ldots$ converting, the ODE to the PDE. The variables and derivatives are changed using this method, as shown in equations (4.3.1) and (4.3.2),

$$\mathbf{v} = \mathbf{v_0} + \epsilon \mathbf{v_1} + \epsilon^2 \mathbf{v_2} + \ldots \tag{4.3.1}$$

$$\frac{d}{dt} = \frac{\partial}{\partial T_0} + \epsilon \frac{\partial}{\partial T_1} + \epsilon^2 \frac{\partial}{\partial T_2} + \ldots \tag{4.3.2}$$

the main governing equation, given in (4.2.13) and (4.2.14), becomes a PDE when the above transformations given in equations (4.3.1) and (4.3.2) are applied to it. The idea now is to separate terms involving various powers of ϵ. The equations are linear in terms of one of the variables $\mathbf{v_0}$, $\mathbf{v_1}$, etc. at the individual powers.

The solution to the first equation, for example, containing variable $\mathbf{v_0}$ at $\epsilon = 0$, can be used as an input force to the second equation, which occurs at $\epsilon = 1$ and contains state variable $\mathbf{v_1}$. The first ODE for $\epsilon = 0$ is usually homogeneous and linear, whereas the others for $\epsilon \geq 1$ are usually non-homogeneous linear. Solving equations with increasing powers of ϵ sequentially reveals all variables involved in any equation involving the power of ϵ. Following the evaluation of some of the variables, such as $\mathbf{v_0}$, $\mathbf{v_1}$ and $\mathbf{v_2}$, the equation (4.3.1) approximates the system.

In applying the method of multiple scales, secular terms in the input force frequently appear, causing the system solution to blow up to infinity if they are not removed. Secular terms are those whose frequency is equal to, or sometimes a sub-multiple of, the system's natural frequency. These terms' coefficients are removed by setting them to zero. This procedure yields amplitude and phase equations, which can be used to plot

frequency response curves.

4.3.1 Application on the Center Manifolds

The system of equations given in (4.2.13) and (4.2.14) can be solved using the method of multiple scales. The variables become $v_2(t) = v_2(t, \epsilon t, \epsilon^2 t \ldots)$, $v_3(t) = v_3(t, \epsilon t, \epsilon^2 t \ldots)$, and thus $v_2(t) = v2(T_0, T_1, T_2 \ldots)$ and $v_3(t) = v3(T_0, T_1, T_2 \ldots)$. Therefore, variable dependence shifts from real-time t to different fast and slow time scales T_0, T_1, T_2,.... In equations (4.3.3), (4.3.4) and (4.3.5), transformations similar to equations (4.3.1) and (4.3.2) are used,

$$v_2 = v_{20} + \epsilon v_{21} + \epsilon^2 v_{22} + O(\epsilon^3) \tag{4.3.3}$$

$$v_3 = v_{30} + \epsilon v_{31} + \epsilon^2 v_{32} + O(\epsilon^3) \quad \textit{and} \tag{4.3.4}$$

$$\frac{d}{dt} = \frac{\partial}{\partial T_0} + \epsilon \frac{\partial}{\partial T_1} + \epsilon^2 \frac{\partial}{\partial T_2} + O(\epsilon^3) \tag{4.3.5}$$

where $O(\epsilon^3)$ refers to the terms of cubic or higher degree powers. The number of differential equations is determined by putting these equations (4.3.3), (4.3.4) and (4.3.5) in the center manifolds equations (4.2.13) and (4.2.14) and comparing both sides of each equation for the same power of ϵ. We have equations for state variables v_{20} and v_{30} at $\epsilon = 0$, but these are the FPs, so we keep $v_{20} = v_{30} = 0$. These equations are enlisted in equations (4.3.6), (4.3.7) and (4.3.8) respectively, for $\epsilon = 1, 2, 3$. The conjugate of these equations are true for the conjugate variables v_{31}, v_{32} *and* v_{33} and are given in (4.3.9), (4.3.10) and (4.3.11) respectively, for the same $\epsilon = 1, 2, 3$

$$\frac{dv_{21}}{dT_0} = \iota\omega v_{21} \tag{4.3.6}$$

$$\frac{dv_{22}}{dT_0} - \iota\omega v_{22} = -\frac{dv_{21}}{dT_1} + c_0\sigma + c_{121}v_{21}^2 + c_{311}v_{21}v_{31} + c_{221}v_{31}^2 \tag{4.3.7}$$

$$\frac{dv_{23}}{dT_0} - \iota\omega v_{23} = F(v_{21}, v_{22}, v_{31}, v_{32}) \tag{4.3.8}$$

$$\frac{dv_{31}}{dT_0} = -\iota\omega v_{31} \tag{4.3.9}$$

$$\frac{dv_{32}}{dT_0} + \iota\omega v_{32} = -\frac{dv_{31}}{dT_1} + \bar{c}_0\sigma + \bar{c}_{121}v_{31}^2 + \bar{c}_{311}v_{31}v_{21} + \bar{c}_{221}v_{21}^2 \tag{4.3.10}$$

$$\frac{dv_{33}}{dT_0} + \iota\omega v_{33} = \bar{F}(v_{21}, v_{22}, v_{31}, v_{32}) \tag{4.3.11}$$

It is possible to solve the linear equations at ϵ^1 given in equation (4.3.6) and (4.3.9), and the solutions of these homogeneous equations are given in equation (4.3.12) and

(4.3.13). There are other equations for variables v_{31}, v_{32} and v_{33} that are similar to equations (4.3.6), (4.3.7) and (4.3.8)but complex conjugate of these equations that are mentioned in equations (4.3.9), (4.3.10) and (4.3.11). Therefore, the variable v_{31}, which is the complex conjugate of v_{21}, has a solution in equation (4.3.13). The symmetry of the two conjugate equations for two conjugate variables is observed during the process of solving equations (4.2.13) and (4.2.14),

$$v_{21}(T_0, T_1, T_2) = A(T_1, T_2)e^{\iota\omega T_0} \tag{4.3.12}$$

$$v_{31}(T_0, T_1, T_2) = \bar{A}(T_1, T_2)e^{-\iota\omega T_0} \tag{4.3.13}$$

equation (4.3.7) is a nonlinear equation of $O(\epsilon^2)$, with variable v_{22} unknown and variables v_{21} and v_{31} known from equations (4.3.12) and (4.3.13). Using these values, v_{21} and v_{31} act as force inputs to the equation (4.3.7), and thus the nonlinear terms are dissolved into known inputs and a linear forced first order equation is obtained, which can be solved. Equation (4.3.14) shows equation (4.3.7) with the values of input variables v_{21} and v_{31} is inserted into the forcing terms. It has a conjugate equation with unknown variable v_{32} given in equation (4.3.10), similar to equation (4.3.7). The nonlinearity is dissolved into forcing inputs using the known variable function from equations (4.3.12) and (4.3.13), and the equation can then be solved,

$$\begin{aligned}\frac{\partial v_{22}}{\partial T_0} - \iota v_{22}\omega =& c_{221}e^{-2iT_0\omega}\bar{A}(T_1, T_2)^2 + c_{311}A(T_1, T_2)\bar{A}(T_1, T_2) \\ &- e^{iT_0\omega}\frac{\partial A}{\partial T_1}(T_1, T_2) + c_{121}e^{2iT_0\omega}A(T_1, T_2)^2 + c_0\sigma\end{aligned} \tag{4.3.14}$$

$$\begin{aligned}\frac{\partial v_{32}}{\partial T_0} + \iota v_{32}\omega =& \bar{c}_{221}e^{2iT_0\omega}A(T_1, T_2)^2 + \bar{c}_{311}\bar{A}(T_1, T_2)A(T_1, T_2) \\ &- e^{-iT_0\omega}\frac{\partial \bar{A}}{\partial T_1}(T_1, T_2) + \bar{c}_{121}e^{-2iT_0\omega}\bar{A}(T_1, T_2)^2 + \bar{c}_0\sigma,\end{aligned} \tag{4.3.15}$$

equation (4.3.14) is created by replacing the values of variables v_{21} and v_{31} from equations (4.3.12) and (4.3.13). The resulting form of the system is shown in equation (4.3.14) and its solution contains the term $T_0 e^{\iota\omega T_0}\frac{dA(T_1,T_2)}{dT_1}$, indicating that the solution will explode over time. This is due to the fact that one of the forcing terms has the same frequency as the natural frequency ω of the corresponding equation, causing resonance. The secular terms containing frequency equal to the system's natural frequency must be eliminated. The coefficients of secular terms are gathered and set to zero for this purpose. This results in the equation (4.3.16) being the solution. The form of the solution

shown in (4.3.18) is obtained by removing the secular term from equation (4.3.14) and solving for its solution.

The same procedure is applied for the conjugate equation (4.3.10) by putting the value of variables v_{21} and v_{31} acting as force and then removing the coefficients of secular terms forming equation (4.3.17). The solution of the equation (4.3.10) after removing the secular terms is given in equation (4.3.19),

$$\frac{dA(T_1,T_2)}{dT_1} = 0 \tag{4.3.16}$$

$$\frac{d\bar{A}(T_1,T_2)}{dT_1} = 0. \tag{4.3.17}$$

The complex conjugate of v_{22} given in (4.3.18) is the solution to variable v_{32}. One obtained at $O(\epsilon^3)$ is equation (4.3.8). This is a first-order equation with an unknown variable v_{23} and a condensed forcing function $F(v_{21},v_{22},v_{31},v_{32})$. The variables v_{21}, v_{22}, v_{31} and v_{32} are known at this point, and inserting these values into the input function $F(v_{21},\ v_{22},\ v_{31},\ v_{32})$ yields a linear forced ODE and after plugging in the values for v_{21}, v_{22}, v_{31} and v_{32}, the coefficients of the newly formed ODE contain secular terms that, when solved, blow up the results. The coefficients of the secular terms $e^{\iota\omega T_0}$ are added together and separated to form the equation (4.3.20), which gives the system's steady state amplitude,

$$\begin{aligned} v_{22}(T_0,T_1,T_2) = &\frac{ic_{311}A(T_1,T_2)\,\bar{A}(T_1,T_2)}{\omega} + \frac{ic_{221}e^{-2iT_0\omega}\bar{A}(T_1,T_2)^2}{3\omega} - \\ &\frac{ic_{121}e^{2iT_0\omega}A(T_1,T_2)^2}{\omega} + \frac{ic_0\sigma}{\omega} \end{aligned} \tag{4.3.18}$$

$$\begin{aligned} v_{32}(T_0,T_1,T_2) = &-\frac{i\bar{c}_{311}\bar{A}(T_1,T_2)\,A(T_1,T_2)}{\omega} - \frac{i\bar{c}_{221}e^{2iT_0\omega}A(T_1,T_2)^2}{3\omega} - \\ &-\frac{i\bar{c}_{121}e^{-2iT_0\omega}\bar{A}(T_1,T_2)^2}{\omega} - \frac{i\bar{c}_0\sigma}{\omega}. \end{aligned} \tag{4.3.19}$$

The complex coefficient $A(T_2) = a(T_2)e^{\iota\beta(T_2)}$ is a function of the amplitude and phase. When this coefficient is expanded in equation (4.3.20), the amplitude equation (4.3.21) and phase equation (4.3.22) are obtained by substituting values for complex constants and separating the real and imaginary parts,

$$\begin{aligned} A'(T_2) = &-\frac{2ic_{221}d_{221}A(T_2)^2\bar{A}(T_2)}{3\omega} - \frac{ic_{311}d_{311}A(T_2)^2\bar{A}(T_2)}{\omega} \\ &+\frac{ic_{121}c_{311}A(T_2)^2\bar{A}(T_2)}{\omega} + c_{321}A(T_2)^2\bar{A}(T_2) - \frac{ic_{311}d_0\sigma A(T_2)}{\omega} \\ &+\frac{2ic_0c_{121}\sigma A(T_2)}{\omega} + c_{112}\sigma A(T_2) \end{aligned} \tag{4.3.20}$$

the normal form of supercritical Hopf bifurcation is represented by the amplitude equation (4.3.21). Allowing $a'(T_2) = 0$ results in an amplitude of $a = \pm 0.51\sqrt{-\sigma}$ in the steady state. This indicates that the periodic solution occurs only when $\sigma < 0$, or the value of the control parameter crosses the Hopf bifurcation point and is less than the critical control parameter i.e., for $H < 7.97$,

$$a'(T_2) = -0.29\sigma a(T_2) - 1.13a(T_2)^3 \tag{4.3.21}$$

$$\gamma'(T_2) = -1.84a(T_2)^2 - 0.16\sigma. \tag{4.3.22}$$

The amplitude equation (4.3.21) can be combined with equations (4.3.3), (4.3.4) and (4.3.12), (4.3.13), where $A = ae^{\iota\beta}$ and the solution to the manifold equations (4.2.13) and (4.2.14) can be obtained by neglecting v_{22} and v_{32} and keeping in mind the values of FPs v_{20} and v_{30}. However, this is a solution to the manifold equations (4.2.13) and (4.2.14), not to the governing equation of the BVAM model (3.1.6).

Following the normal forms given in equations (4.3.21) and (4.3.22) at $H = 7.97$, reverse transformation to the one done in section (4.2) of center manifolds reduction is required to get the response for BVAM model given in equation (3.1.6) in the local region of Hopf bifurcation. The analytical solution for the original BVAM model in the local region of Hopf bifurcation at $H = 7.97$ is obtained after that transformation.

4.3.2 Reverse Transformation

As mentioned before, a change of transformation is needed to go back to the original coordinates. This transformation will be in exact reverse to the transformation that was done to transform the original coordinates $\mathbf{x}$ to the manifold coordinates $\mathbf{v}$. Since we know for transforming original coordinates, the first transformation was done to translate the coordinate axis from $\mathbf{x}$ to FP $\mathbf{x_0}$ where the state variable becomes $\mathbf{y}$. This transformation is shown in the equation (4.2.1). After that, a transformation was done to transform the translated coordinates $\mathbf{y}$ to manifold coordinates $\mathbf{v}$ as shown in equation (4.2.4). Following the exact steps backward, one can go back from the manifold coordinates $\mathbf{v}$ to the original coordinates $\mathbf{x}$.

First of all the solution is formed using the equation (4.3.12), (4.3.13) and inserting the values of steady-state phases and amplitudes from equation (4.3.21) and (4.3.22). Values of v_2 and v_3 is formed using equation (4.3.3) and equation (4.3.4).

Once the values of v_2 and v_3 are known, variables v_1 and v_4 can be determined using

the equation (4.2.12) with coefficient given in table (4.1). This equation (4.2.12) was the approximation of stable manifolds in terms of center manifold variables.

With v_1, ,v_2, ,v_3, ,v_4 all known, the vector $\mathbf{v}$ is determined. So a transformation is required to shift from $\mathbf{v}$ coordinates to $\mathbf{y}$ coordinates using the equation (4.2.4). In that way the variable $\mathbf{y}$ is determined. Now next transformation is a simple translation back of axis from $\mathbf{y}$ coordinates to $\mathbf{x}$ using the equation (4.2.1). After following all these transformations one arrive at the solution that is applicable at the original coordinates $\mathbf{x}$. The solution form is given in equation (4.3.23),

$$\mathbf{x} = \mathbf{x_0} + \mathbf{a_1}\sigma + \epsilon^2\mathbf{a_2}\sigma + \epsilon\mathbf{a_3}\sqrt{\sigma}\sin\left[(\omega_1 + \epsilon^2 c_1\sigma)t + \boldsymbol{\beta_1}\right] + \epsilon^2\mathbf{a_4}\sigma\sin\left[(\omega_2 + \epsilon^2 c_2\sigma)t + \boldsymbol{\beta_2}\right] \tag{4.3.23}$$

and it can be seen that from the FP $\mathbf{x_0}$, the amplitude of the analytical solution of equation (4.3.23) solution gradually increases. The FPs change as the control parameter is varied, as can be seen in the second and third terms of the analytical solution. The coefficients $\mathbf{a_1}$, $\mathbf{a_2}$, $\mathbf{a_3}$, $\mathbf{a_4}$, $\boldsymbol{\beta_1}$ and $\boldsymbol{\beta_2}$ are vectors, and the value of their components corresponds to the different components of variable $\mathbf{x}$ which are x_1, x_2, x_3 and x_4. Therefore, it is clear that all of the components of $\mathbf{x}$ have different amplitudes and phase differences.

Chapter 5

Results and Discussion

A comprehensive analytical analysis is done on the BVAM model. In order to approximate the analytical solution of the BVAM model at a specific control parameter value, and analyze its behavior in the local region to that specific value of control parameter, the method of multiple scales is used which is a perturbation technique to approximate an analytical solution to nonlinear differential equations.
Direct application of the method of multiple scales was not possible, since the model of the system has multiple solutions at specific control parameters. Therefore, the analysis is focused on one specific fixed point and its local region. A transformation to manifolds was performed so that the right kind of solution is separated.

5.1 Identification of Hopf Bifurcation Points

In this thesis work, analytical techniques for nonlinear dynamical systems were performed to first find out some of the points where bifurcations are happening and then the analytical solution is approximated in the local region to Hopf bifurcation. The system is linearized to find out the Jacobian matrix whose eigenvalues gave information about the stability and help in identifying possible points of Hopf bifurcation. Table (3.3) and table (3.4) show the eigenvalues of the Jacobian matrix near two fixed points $H = 8.77$ and $H = 7.97$. It is indicated that the former two points are the points of Hopf bifurcation. The real part of eigenvalues was negative for the control parameter value greater than the critical value of the control parameter indicating stable fixed points.

For a control parameter value less than the critical value of the control parameter the fixed points become unstable and the real part of the eigenvalues of the Jacobian matrix became positive. At the Hopf bifurcation point, the real part of eigenvalues was zero but an imaginary part was introduced which added a frequency of oscillation to the system. For control parameter $H > 8.77$ there were two stable fixed points and one unstable trivial fixed point. The two stable fixed points are given in table (3.1) at $H = 9$. For $7.97 < H \leq 8.77$ there are two unstable fixed points, one stable fixed point along with a stable periodic solution that has emerged from $H = 8.77$. At the end for $H < 7.97$, there are three unstable fixed points and two stable periodic solutions that are emerged from $H = 8.77$ and $H = 7.97$.

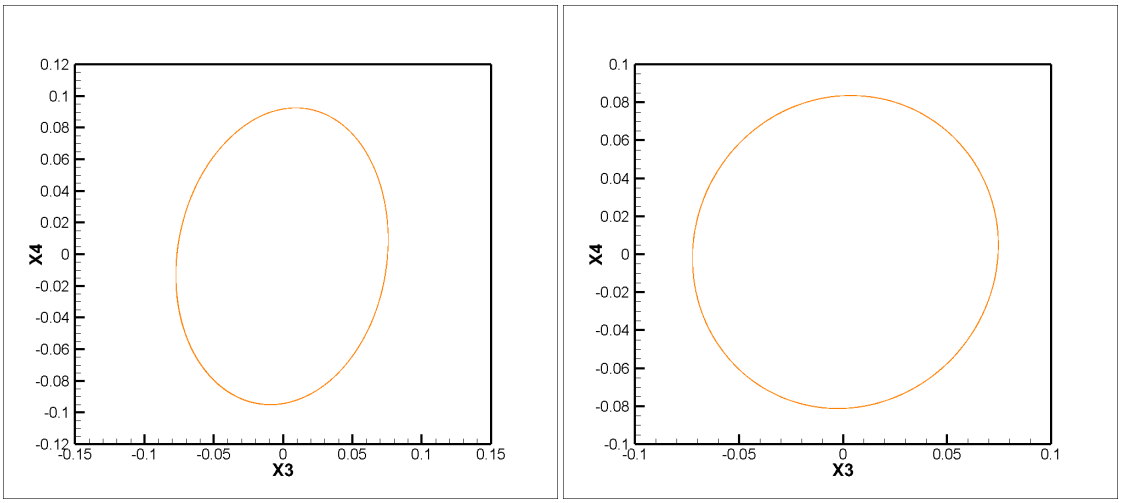

(a) Phase portrait for the periodic solution after Hopf bifurcation at H = 8.75

(b) Phase portrait for the periodic solution after Hopf bifurcation at H = 7.95

Figure 5.1: Phase portraits in the local region to Hopf bifurcations

5.2 Identification of Period Doubling Bifurcation Points

The periodic solution can be seen to have a distinct change in phase portrait around $H \approx 4.625$. The trajectory in phase space is folded on itself twice before closing (see figure (5.2)). Nonlinear analysis is performed in this region of the control parameter to identify the possible point of period-doubling bifurcation.

For periodic solutions, the Floquet multipliers provide the information about the stabil-

ity of the solution. Floquet multipliers are the eigenvalues of the monodromy matrix. These eigenvalues tell about if a solution will diverge or converge from the path of a periodic solution. The Floquet multipliers of absolute value 1 show the periodic nature of the solution. Another Floquet multiplier of value less than absolute 1 represents that the solution will eventually converge to a periodic solution. However, the Floquet multipliers greater than absolute 1 show the instability of that periodic solution.

For a periodic solution, there can be different scenarios of how a Floquet multiplier

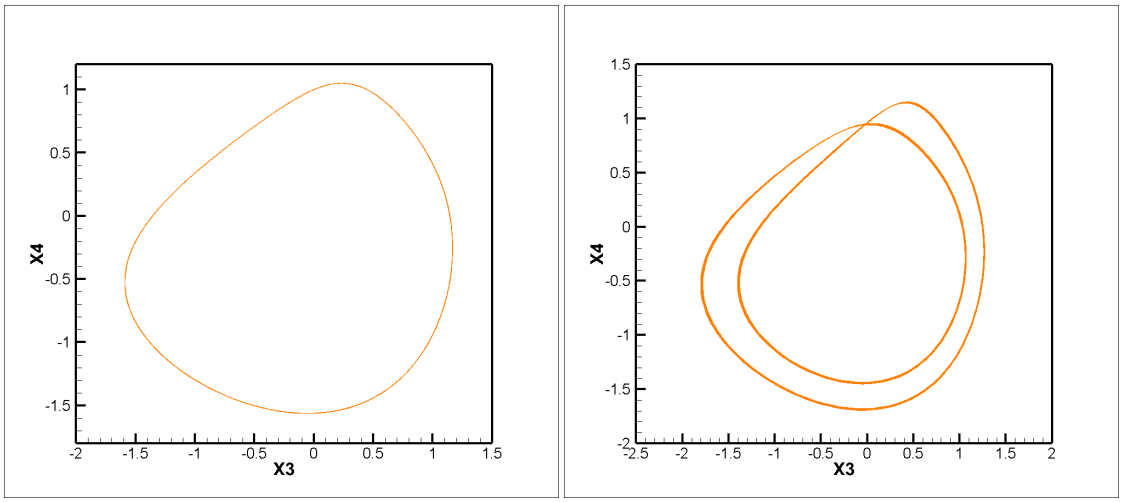

(a) Phase portrait for the first periodic solution before period-doubling bifurcation at H = 4.630 (b) Phase portrait for the first periodic solution after period-doubling bifurcation at H = 4.620

Figure 5.2: Phase portraits before and after $H = 4.625$

leaves a unit circle in a complex plane. In each scenario, a different bifurcation can happen. Table (3.5) shows that for the control parameter value greater than 4.625, all the Floquet multipliers except one are inside the unit circle. One of the Floquet multipliers is always at a unit circle circumference with the value of 1. However, at value $H \approx 4.625$, there are two Floquet multipliers at the unit circle, one at 1, and the other has the value of -1. For control parameter values $H < 4.625$ the Floquet multiplier of value -1 leaves the unit circle. Therefore from now onward, this periodic solution becomes unstable. The pattern of how a Floquet multiplier is leaving the unit circle suggests that the type of bifurcation happening is period-doubling bifurcation.

To confirm this result, Poincare section is plotted at the corresponding values of the control parameter. An intersection of this plane is taken with the trajectory in the phase plane after every time period T. So for every periodic solution, it is evident that the

Poincare section will consist of one single dot. Therefore, in figure (5.3a) the Poincare section shows a single dot at $H = 4.63$ indicating a single period, periodic solution. However, at $H = 4.62$, we see two dots in the Poincare section in figure (5.3b). Since by definition since Poincare section is the intersection of the hyper-plane with the phase plane after every time period and we are seeing two dots for the span of one time period T, it means that the time period of this system is essentially doubled. A similar conclu-

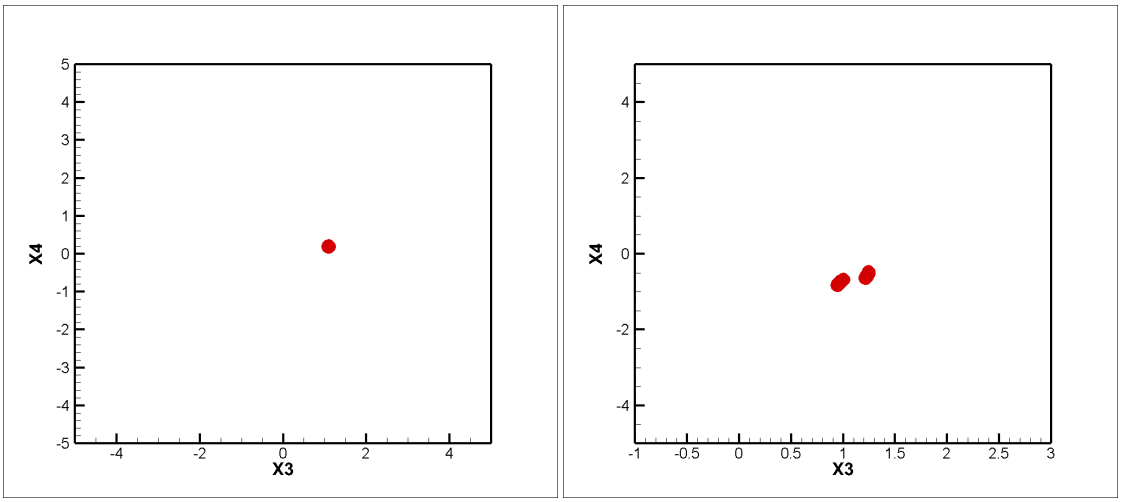

(a) Poincare section for the first periodic solution prior to period-doubling bifurcation at H = 4.630

(b) Poincare section for the first periodic solution after period-doubling bifurcation at H = 4.620

Figure 5.3: Poincare sections before and after $H = 4.625$

sion is made for the other periodic solution. Following table (3.6), it is observed that the second stable periodic solution becomes unstable and undergoes period-doubling bifurcation at control parameter value $H = 4.565$. Now after, $H < 4.565$ there are three unstable fixed points, two unstable periods one solution, and two stable periodic solutions.

5.3 Analytical Solution

the analytical solution is found in the local region to Hopf bifurcation. After transforming the system to its center manifold and decoupling the center manifold from stable manifolds as is done in section 4, an analytical solution is found using the method of

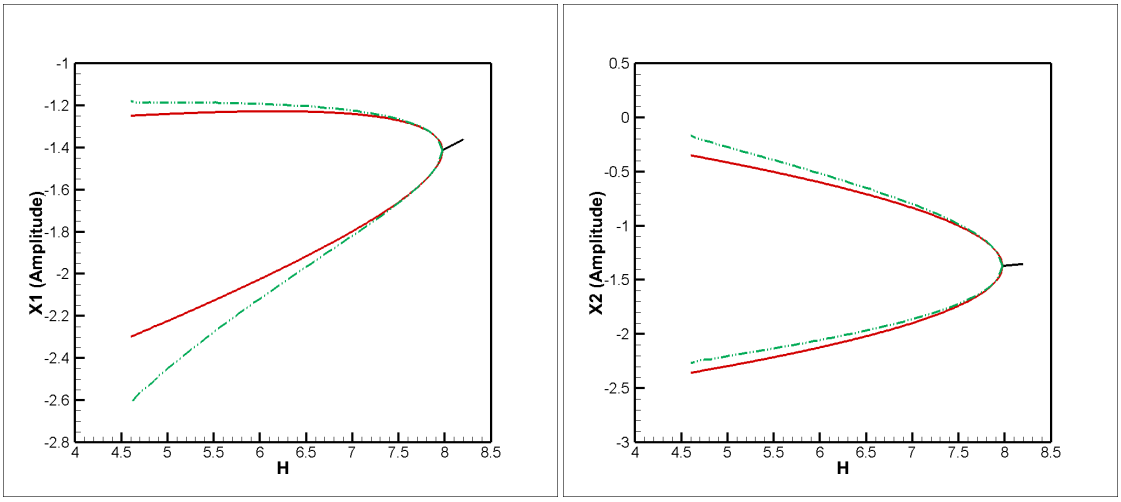

(a) Amplitude comparison for x_1 (b) Amplitude comparison for x_2

Figure 5.4: Comparison of analytical and numerical amplitudes for state variables $\mathbf{x}$ for equation (3.1.6) upon variation control parameter H

multiple scales. The amplitude and phase equations (4.3.21) and (4.3.22) represent the change in amplitude and phase with the control parameter value. However, this change can be visualized but it cannot be compared to see the numerical solution since this amplitude is in the coordinates of manifolds $\mathbf{v}$ and the numerical solution is only available in original coordinates $\mathbf{x}$. A reverse transformation was also applied in the previous section to attain the analytical solution of the system which is given in equation (4.3.23). From this solution, the time-varying cosines and sines are assumed to be 1 and in this way, the other terms sum up to represent the actual amplitude of the system in $\mathbf{x}$. These two amplitudes i.e. amplitude obtained through analytical consideration (equation (4.3.23)) compared with the amplitude obtained numerically. The comparison is done with the variation of the control parameter H value. Figures (5.4) and (5.5) shows this comparison. Comparison of analytical amplitude obtained from equation (4.3.23) with the numerical solution shows that the analytical solution to the system of equation is accurate up to a finite value of control parameter away from the Hopf bifurcation. After a certain value control parameter, the two solution amplitudes diverge from each other. This is the limit of analytical solutions that cannot be computed accurately for more than a certain limit. However, the amplitude equation is giving a good insight into the nature of the system.

The power spectrum of the BVAM model is shown in the local region to Hopf bifurca-

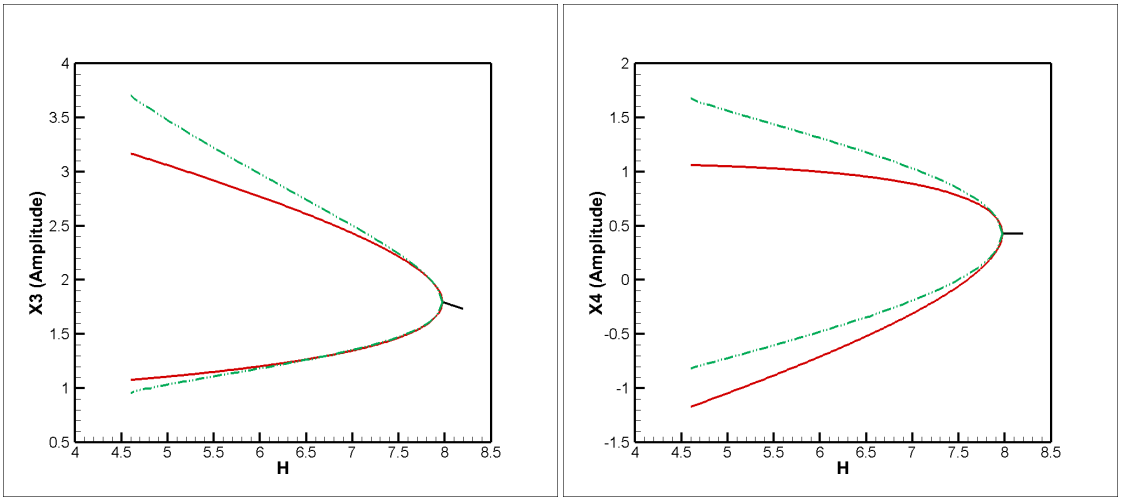

(a) Amplitude comparison for x_3 (b) Amplitude comparison for x_4

Figure 5.5: Comparison of analytical and numerical amplitudes for state variables $\mathbf{x}$ for equation (3.1.6) upon variation control parameter H

tion at $H = 7.95$ in figure (7.1) in the appendix. The spectrum shows three dominant frequencies as evident the system has cubic non-linearity. The frequencies obtained analytically are $H_c - \sigma = 7.97$. At $H = 7.95$ the first dominant frequency is $\omega_1 + \epsilon^2 c_1 \sigma$ and the second dominant frequency is $\omega_2 + \epsilon^2 c_2 \sigma$. The parameter values are given in equation (**??**). Filling these values gives us the frequency values to be $5.55\,rad/s$ and $11.10\,rad/s$. Numerically from the power spectrum, these values are close to $5.2\,rad/s$ and $10.4\,rad/s$. Although these frequencies are not exact, there is a slight amount of error between the values of frequencies calculated analytically and numerically. However, calculation analytically provide us with the relationship of how a frequency can change upon varying control parameter.

Chapter 6

Conclusion

6.1 Summary of Current Work

The heart is a vital organ in the human body however, according to an engineering perspective it is a mechanical pump that is actuated by electrical pulses. These electrical pulses make the walls of the heart stretch and contract in such a way that blood gets flowed into the whole body. While this phenomenon is happening, electrical charges get placed at different locations of the body having definite values of potential when measured over time, it forms a specific wave. This is referred to as an ECG of the heart. This ECG is different with different conditions of the heart. A very recent paper presents a mathematical model which reproduces ECGs of healthy and abnormal hearts and the route from normal sinus rhythm to arrhythmia validates the actual path followed.

This model is referred to as a discretized version of the BVAM model. The BVAM model has several types of solutions at different values of parameters. It has fixed point solutions, periodic and multi-period solutions and quasi-periodic solutions, and chaotic solutions. Bifurcation happens when one type of solution changes to another type of solution with a varying control parameter value. The BVAM model has three fixed point solutions for control parameter value less than 8.77 where two FP are stable and the trivial solution representing origin is unstable. The Hopf bifurcation occurs at the control parameter value of 8.77 and 7.97 for the two stable FPs and turns them into periodic solutions. We formed an analytical solution in the local region to Hopf bifurcation. This periodic solution changes into a period-two solution at the mentioned control parameter values of period-doubling bifurcation. ECG of the heart lies in one

of the branches of solution which emerged as the solution kept changing its types from fixed point solution to multi-period solution. Further bifurcation brings solution into the chaotic region where we observe atrial fibrillation which is one of the malignant arrhythmia of the heart.

6.2 Future Work

Current thesis work is limited to finding two of the bifurcation points and forming an analytical solution in the local region to the Hopf bifurcation only. This is applicable on many natural phenomena related to biology however, the ECG of human body lies near the chaotic and quasi-periodic region. The route towards chaos is known to be Ruelle–Takens–Newhouse route to chaos. Although it may be difficult to find analytical solution near this region however, appropriate system identification tools can be used to associate the parameters of BVAM model to ECG of the heart.

Chapter 7

Appendix

Equation (4.2.7)

$$
\begin{aligned}
v_1'(t) = &-(0.241519 - 0.222009i)\sigma v_2(t) - (0.241519 + 0.222009i)\sigma v_3(t) \\
&+ (0.57831 + 0.612048i)v_2(t)v_1(t)^2 + (0.57831 - 0.612048i)v_3(t)v_1(t)^2 \\
&+ (1.14885 + 1.61151i)v_2(t)^2 v_1(t) + (1.14885 - 1.61151i)v_3(t)^2 v_1(t) \\
&- (2.26337 + 2.84244i)v_2(t)v_1(t) - (2.26337 - 2.84244i)v_3(t)v_1(t) \\
&+ (0.993279 + 0.868225i)v_2(t)v_4(t)v_1(t) + (0.993279 - 0.868225i)v_3(t)v_4(t)v_1(t) \\
&- (0.260007 - 0.424567i)v_2(t)^3 - (0.260007 + 0.424567i)v_3(t)^3 - (3.8589 + 1.68177i)v_2(t)^2 \\
&- (0.178819 + 0.315926i)v_2(t)v_3(t)^2 - (3.8589 - 1.68177i)v_3(t)^2 \\
&+ (0.279673 + 0.327613i)v_2(t)v_4(t)^2 + (0.279673 - 0.327613i)v_3(t)v_4(t)^2 \\
&- (0.178819 - 0.315926i)v_2(t)^2 v_3(t) + (1.45039 + 1.05599i)v_2(t)^2 v_4(t) \\
&+ (1.45039 - 1.05599i)v_3(t)^2 v_4(t) - (1.38617 + 2.18671i)v_2(t)v_4(t) \\
&- (1.38617 - 2.18671i)v_3(t)v_4(t) - 5.41348\sigma + 1.00081\sigma v_1(t) + 1.5962\sigma v_4(t) + 0.84583v_1(t)^3 \\
&+ 2.55533v_4(t)v_1(t)^2 - 6.72024v_1(t)^2 + 2.43107v_4(t)^2 v_1(t) + 1.68556v_2(t)v_3(t)v_1(t) \\
&- 12.2344v_4(t)v_1(t) - 7.49796v_1(t) + 0.752717v_4(t)^3 - 5.46495v_4(t)^2 \\
&- 7.42918v_2(t)v_3(t) + 2.40363v_2(t)v_3(t)v_4(t)
\end{aligned}
$$

$$
\begin{aligned}
v_2'(t) =&(0.30014 - 0.163536i)\sigma + (0.0282701 + 0.0531356i)\sigma v_1(t) \\
&- (0.00979015 - 0.334817i)\sigma v_2(t) + (0.186253 - 0.308481i)\sigma v_3(t) \\
&- (0.00149033 - 0.0720104i)\sigma v_4(t) - (0.0748609 - 0.434152i)v_2(t)v_1(t)^2 \\
&+ (0.335977 + 0.331142i)v_3(t)v_1(t)^2 - (0.0620415 - 0.219681i)v_4(t)v_1(t)^2 \\
&+ (0.187056 - 0.522723i)v_1(t)^2 - (0.304132 + 0.0318502i)v_2(t)^2 v_1(t) \\
&+ (0.137781 - 0.025187i)v_3(t)^2 v_1(t) \\
&- (0.0908968 - 0.135614i)v_4(t)^2 v_1(t) - (0.437948 + 2.34955i)v_2(t)v_1(t) \\
&- (0.0659915 - 0.0871909i)v_2(t)v_3(t)v_1(t) - (1.31142 + 2.32047i)v_3(t)v_1(t) \\
&+ (0.043977 + 0.920467i)v_2(t)v_4(t)v_1(t) + (0.578765 + 0.795192i)v_3(t)v_4(t)v_1(t) \\
&+ (0.457912 - 0.681398i)v_4(t)v_1(t) - (0.110516 - 0.114752i)v_2(t)^3 \\
&+ (0.205373 + 0.0298759i)v_3(t)^3 - (0.0391608 - 0.0166236i)v_4(t)^3 \\
&+ (0.79171 - 0.137661i)v_2(t)^2 + (0.22726 + 0.0150395i)v_2(t)v_3(t)^2 \\
&- (0.31667 - 0.136479i)v_3(t)^2 + (0.0894677 + 0.45013i)v_2(t)v_4(t)^2 \\
&+ (0.253637 + 0.419201i)v_3(t)v_4(t)^2 + (0.267918 - 0.158453i)v_4(t)^2 \\
&+ (0. + 5.56511i)v_2(t) - (0.139824 - 0.135539i)v_2(t)^2 v_3(t) \\
&+ (0.427722 - 0.0691838i)v_2(t)v_3(t) - (0.250396 + 0.00723305i)v_2(t)^2 v_4(t) \\
&+ (0.062812 - 0.0131308i)v_3(t)^2 v_4(t) - (0.650968 + 2.19451i)v_2(t)v_4(t) \\
&- (0.106076 - 0.0967724i)v_2(t)v_3(t)v_4(t) - (1.11413 + 2.26283i)v_3(t)v_4(t) \\
&+ (-0.0112774 + 0.0940332i)v_1(t)^3
\end{aligned}
$$

$$
\begin{aligned}
v_3'(t) =& (0.30014 + 0.163536i)\sigma + (0.0282701 - 0.0531356i)\sigma v_1(t) \\
&+ (0.186253 + 0.308481i)\sigma v_2(t) - (0.00979015 + 0.334817i)\sigma v_3(t) \\
&- (0.00149033 + 0.0720104i)\sigma v_4(t) + (0.335977 - 0.331142i)v_2(t)v_1(t)^2 \\
&- (0.0748609 + 0.434152i)v_3(t)v_1(t)^2 - (0.0620415 + 0.219681i)v_4(t)v_1(t)^2 \\
&+ (0.187056 + 0.522723i)v_1(t)^2 + (0.137781 + 0.025187i)v_2(t)^2v_1(t) \\
&- (0.304132 - 0.0318502i)v_3(t)^2v_1(t) - (0.0908968 + 0.135614i)v_4(t)^2v_1(t) \\
&- (1.31142 - 2.32047i)v_2(t)v_1(t) - (0.0659915 + 0.0871909i)v_2(t)v_3(t)v_1(t) \\
&- (0.437948 - 2.34955i)v_3(t)v_1(t) + (0.578765 - 0.795192i)v_2(t)v_4(t)v_1(t) \\
&+ (0.043977 - 0.920467i)v_3(t)v_4(t)v_1(t) + (0.457912 + 0.681398i)v_4(t)v_1(t) \\
&+ (0.205373 - 0.0298759i)v_2(t)^3 - (0.110516 + 0.114752i)v_3(t)^3 \\
&- (0.0391608 + 0.0166236i)v_4(t)^3 - (0.31667 + 0.136479i)v_2(t)^2 \\
&- (0.139824 + 0.135539i)v_2(t)v_3(t)^2 + (0.79171 + 0.137661i)v_3(t)^2 \\
&+ (0.253637 - 0.419201i)v_2(t)v_4(t)^2 + (0.0894677 - 0.45013i)v_3(t)v_4(t)^2 \\
&+ (0.267918 + 0.158453i)v_4(t)^2 + (0.22726 - 0.0150395i)v_2(t)^2v_3(t) \\
&+ (0.427722 + 0.0691838i)v_2(t)v_3(t) - (0. + 5.56511i)v_3(t) \\
&+ (0.062812 + 0.0131308i)v_2(t)^2v_4(t) - (0.250396 - 0.00723305i)v_3(t)^2v_4(t) \\
&- (1.11413 - 2.26283i)v_2(t)v_4(t) - (0.106076 + 0.0967724i)v_2(t)v_3(t)v_4(t) \\
&- (0.650968 - 2.19451i)v_3(t)v_4(t) + (-0.0112774 - 0.0940332i)v_1(t)^3
\end{aligned}
$$

$$
\begin{aligned}
v_4'(t) =&(0.181794 - 0.0145951i)\sigma v_2(t) + (0.181794 + 0.0145951i)\sigma v_3(t) \\
&- (0.371626 + 0.487084i)v_2(t)v_1(t)^2 - (0.371626 - 0.487084i)v_3(t)v_1(t)^2 \\
&- (1.10889 + 1.43283i)v_2(t)^2 v_1(t) - (1.10889 - 1.43283i)v_3(t)^2 v_1(t) \\
&+ (1.06091 + 2.50517i)v_2(t)v_1(t) + (1.06091 - 2.50517i)v_3(t)v_1(t) \\
&- (0.544012 + 0.702237i)v_2(t)v_4(t)v_1(t) - (0.544012 - 0.702237i)v_3(t)v_4(t)v_1(t) \\
&+ (0.281913 - 0.330622i)v_2(t)^3 + (0.281913 + 0.330622i)v_3(t)^3 \\
&+ (3.67938 + 1.34322i)v_2(t)^2 + (0.205895 + 0.214997i)v_2(t)v_3(t)^2 \\
&+ (3.67938 - 1.34322i)v_3(t)^2 - (0.0624146 + 0.27382i)v_2(t)v_4(t)^2 \\
&- (0.0624146 - 0.27382i)v_3(t)v_4(t)^2 + (0.205895 - 0.214997i)v_2(t)^2 v_3(t) \\
&- (1.3878 + 0.933346i)v_2(t)^2 v_4(t) - (1.3878 - 0.933346i)v_3(t)^2 v_4(t) \\
&+ (0.274437 + 1.97631i)v_2(t)v_4(t) + (0.274437 - 1.97631i)v_3(t)v_4(t) \\
&+ 3.43956\sigma - 0.604166\sigma v_1(t) - 0.981228\sigma v_4(t) - 0.762353v_1(t)^3 \\
&- 2.3334v_4(t)v_1(t)^2 + 6.16244v_1(t)^2 - 2.25442v_4(t)^2 v_1(t) \\
&- 1.5663v_2(t)v_3(t)v_1(t) + 11.3459v_4(t)v_1(t) - 0.709943v_4(t)^3 + 5.13664v_4(t)^2 \\
&+ 7.0516v_2(t)v_3(t) - 2.2465v_2(t)v_3(t)v_4(t) - 3.35868v_4(t)
\end{aligned}
$$

Coefficients for equations (4.2.13) and (4.2.14)

$c_0 = 0.30014 - 0.163536i, c_{112} = -0.360237 - 0.216171i, c_{121} = 0.79171 - 0.137661i$

$c_{122} = -0.00716157 + 0.0146752i, c_{131} = -0.322004 + 0.394762i, c_{132} = 0.00629063 - 0.0465835i$

$, c_{212} = -0.00786543 - 0.95043i, c_{221} = -0.31667 + 0.136479i, c_{222} = -0.0974716 + 0.0441227i$

$, c_{231} = 0.54642 + 0.10721i, c_{232} = -0.0279866 - 0.0221947i, d_0 = 0.30014 + 0.163536i,$

$d_{112} = -0.00786543 + 0.95043i, d_{121} = -0.31667 - 0.136479i, d_{122} = -0.0974716 - 0.0441227i$

$d_{131} = 0.54642 - 0.10721i, d_{132} = -0.0279866 + 0.0221947i, d_{212} = -0.360237 + 0.216171i$

$d_{221} = 0.79171 + 0.137661i, d_{222} = -0.0072 - 0.01468\iota, d_{231} = -0.322004 - 0.394762i$

$d_{232} = 0.00629063 + 0.0465835i, \omega = 5.56511, c_{311} = 0.427722 - 0.0691838i,$

$c_{312} = 0.168833 + 0.429731i, c_{321} = -1.16988 - 1.90762i, c_{322} = 0.178467 + 0.186764i$

$c_{331} = -0.632278 - 2.36005i, c_{332} = 0.080681 + 0.247657i, d_{311} = 0.427722 + 0.0691838i$

$d_{312} = 0.168833 - 0.429731i, d_{321} = -1.16988 + 1.90762i,$

$d_{322} = 0.178467 - 0.186764i, d_{331} = -0.632278 + 2.36005i, d_{332} = 0.080681 - 0.247657\iota$

Equations (4.3.8)

$$
\begin{aligned}
F(v_{21}, v_{22}, v_{31}, v_{32}) = &- \frac{\mathrm{dv_{21}}}{\mathrm{dT_2}}(T_0, T_1, T_2) - \frac{\mathrm{dv_{22}}}{\mathrm{dT_1}}(T_0, T_1, T_2) + c_{112}\sigma v_{21}(T_0, T_1, T_2) + c_{212}\sigma v_{31}(T_0, T_1, T_2) \\
&+ c_{131} v_{21}(T_0, T_1, T_2)^3 + c_{321} v_{31}(T_0, T_1, T_2) v_{21}(T_0, T_1, T_2)^2 \\
&+ c_{331} v_{31}(T_0, T_1, T_2)^2 v_{21}(T_0, T_1, T_2) + 2c_{121} v_{22}(T_0, T_1, T_2) v_{21}(T_0, T_1, T_2) \\
&+ c_{311} v_{22}(T_0, T_1, T_2) v_{21}(T_0, T_1, T_2) + c_{231} v_{31}(T_0, T_1, T_2)^3 \\
&+ 2c_{221} v_{22}(T_0, T_1, T_2) v_{31}(T_0, T_1, T_2) + c_{311} v_{22}(T_0, T_1, T_2) v_{31}(T_0, T_1, T_2)
\end{aligned}
$$

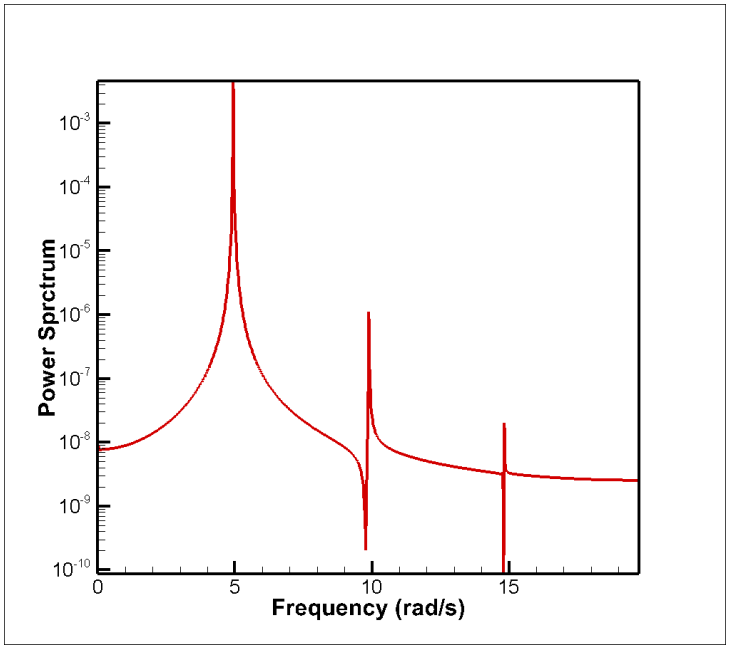

Figure 7.1: Power spectrum simulated numerically at $H = 7.95$ for equation (3.1.6)

Parameters for Analytic Solution given in equation (4.3.23)

$$\mathbf{a_1} = \begin{bmatrix} 0.212308 \\ 0.122757 \\ -0.342036 \\ 0.0214689 \end{bmatrix} \quad \mathbf{a_2} = \begin{bmatrix} 0.135121 \\ 0.131086 \\ -0.23636 \\ -0.0763403 \end{bmatrix} \quad \mathbf{a_3} = \begin{bmatrix} 0.281731 \\ 0.535615 \\ 0.540988 \\ 0.607102 \end{bmatrix} \quad \boldsymbol{a_4} = \begin{bmatrix} 0.0323221 \\ 0.0305694 \\ 0.051652 \\ 0.0461832 \end{bmatrix}$$

$$\boldsymbol{\beta_1} = \begin{bmatrix} 1.07987 \\ -0.318365 \\ 1.52798 \\ 0 \end{bmatrix} \quad \boldsymbol{\beta_2} = \begin{bmatrix} 0.310676 \\ -0.744948 \\ 0.128051 \\ 1.46583 \end{bmatrix}$$

$$c_1 = 0.307995 \quad c_2 = 0.615991 \quad \omega_1 = 5.56 \quad \omega_2 = 11.12$$

References

[1] John E Hall and Michael E Hall. *Guyton and Hall textbook of medical physiology e-Book*. Elsevier Health Sciences, 2020.

[2] Balth Van Der Pol and Jan Van Der Mark. Lxxii. the heartbeat considered as a relaxation oscillation, and an electrical model of the heart. *The London, Edinburgh, and Dublin Philosophical Magazine and Journal of Science*, 6(38):763–775, 1928.

[3] RH Keldermann, MP Nash, and AV Panfilov. Modeling cardiac mechano-electrical feedback using reaction-diffusion-mechanics systems. *Physica D: Nonlinear Phenomena*, 238(11-12):1000–1007, 2009.

[4] Elena Ryzhii and Maxim Ryzhii. A heterogeneous coupled oscillator model for simulation of ecg signals. *Computer methods and programs in biomedicine*, 117(1): 40–49, 2014.

[5] MA Quiroz-Juarez, R Vázquez-Medina, E Ryzhii, M Ryzhii, and JL Aragón. Quasiperiodicity route to chaos in cardiac conduction model. *Communications in Nonlinear Science and Numerical Simulation*, 42:370–378, 2017.

[6] Ali H Nayfeh and Balakumar Balachandran. *Applied nonlinear dynamics: analytical, computational, and experimental methods*. John Wiley & Sons, 2008.

[7] E.J.D.S. Luz, W.R. Schwartz, G. Cámara-Chávez, and D. Menotti. Ecg-based heartbeat classification for arrhythmia detection: A survey. *Computer Methods and Programs in Biomedicine*, 127:144–164, 2016. doi: 10.1016/j.cmpb.2015.12.008. cited By 394.

[8] K. Christensen, K.A. Manani, and N.S. Peters. Simple model for identifying critical regions in atrial fibrillation. *Physical Review Letters*, 114(2), 2015. doi: 10.1103/PhysRevLett.114.028104. cited By 26.

[9] Z. Qu, G. Hu, A. Garfinkel, and J.N. Weiss. Nonlinear and stochastic dynamics in the heart. *Physics Reports*, 543(2):61–162, 2014. doi: 10.1016/j.physrep.2014.05.002. cited By 105.

[10] K.H.W.J.T. Tusscher and A.V. Panfilov. Modelling of the ventricular conduction system. *Progress in Biophysics and Molecular Biology*, 96(1-3):152–170, 2008. doi: 10.1016/j.pbiomolbio.2007.07.026. cited By 98.

[11] P.E. McSharry, G.D. Clifford, L. Tarassenko, and L.A. Smith. A dynamical model for generating synthetic electrocardiogram signals. *IEEE Transactions on Biomedical Engineering*, 50(3):289–294, 2003. doi: 10.1109/TBME.2003.808805. cited By 796.

[12] M. Gidea, C. Gidea, and W. Byrd. Deterministic models for simulating electrocardiographic signals. *Communications in Nonlinear Science and Numerical Simulation*, 16(10):3871–3880, 2011. doi: 10.1016/j.cnsns.2011.01.022. cited By 16.

[13] A.M. Dos Santos, S.R. Lopes, and R.L. Viana. Rhythm synchronization and chaotic modulation of coupled van der pol oscillators in a model for the heartbeat. *Physica A: Statistical Mechanics and its Applications*, 338(3-4):335–355, 2004. doi: 10.1016/j.physa.2004.02.058. cited By 55.

[14] Y. Zhao, J. Sun, and M. Small. Evidence consistent with deterministic chaos in human cardiac data: Surrogate and nonlinear dynamical modeling. *International Journal of Bifurcation and Chaos*, 18(1):141–160, 2008. doi: 10.1142/S0218127408020197. cited By 19.

[15] A. Abdelkefi, Z. Yan, and M.R. Hajj. Nonlinear dynamics of galloping-based piezoaeroelastic energy harvesters. *European Physical Journal: Special Topics*, 222(7):1483–1501, 2013. doi: 10.1140/epjst/e2013-01940-x. URL https://www.scopus.com/inward/record.uri?eid=2-s2.0-84884570307&doi=10.1140%2fepjst%2fe2013-01940-x&partnerID=40&md5=64531a717b97b1b058b22ca3ebd49620. cited By 17.

[16] Alan L Hodgkin and Andrew F Huxley. A quantitative description of membrane current and its application to conduction and excitation in nerve. *The Journal of physiology*, 117(4):500–544, 1952.

[17] Denis Noble. A modification of the hodgkin—huxley equations applicable to purkinje fibre action and pacemaker potentials. *The Journal of physiology*, 160(2): 317–352, 1962.

[18] Ching-hsing Luo and Yoram Rudy. A dynamic model of the cardiac ventricular action potential. i. simulations of ionic currents and concentration changes. *Circulation research*, 74(6):1071–1096, 1994.

[19] Marc Courtemanche, Rafael J Ramirez, and Stanley Nattel. Ionic mechanisms underlying human atrial action potential properties: insights from a mathematical model. *American Journal of Physiology-Heart and Circulatory Physiology*, 275(1): H301–H321, 1998.

[20] Kirsten HWJ ten Tusscher, Denis Noble, Peter-John Noble, and Alexander V Panfilov. A model for human ventricular tissue. *American Journal of Physiology-Heart and Circulatory Physiology*, 286(4):H1573–H1589, 2004.

[21] Neil J Vickers. Animal communication: when i'm calling you, will you answer too? *Current biology*, 27(14):R713–R715, 2017.

[22] Krzysztof Grudziński and Jan J Żebrowski. Modeling cardiac pacemakers with relaxation oscillators. *Physica A: statistical Mechanics and its Applications*, 336 (1-2):153–162, 2004.

[23] Sandra RFSM Gois and Marcelo A Savi. An analysis of heart rhythm dynamics using a three-coupled oscillator model. *Chaos, Solitons & Fractals*, 41(5):2553–2565, 2009.

[24] Carl Zetterberg and Torsten Öfverholm. Carpal tunnel syndrome and other wrist/hand symptoms and signs in male and female car assembly workers. *International Journal of Industrial Ergonomics*, 23(3):193–204, 1999.

[25] L Karthik, Gaurav Kumar, Tarun Keswani, Arindam Bhattacharyya, S Sarath Chandar, and KV Bhaskara Rao. Protease inhibitors from marine actinobacteria as a potential source for antimalarial compound. *PloS one*, 9(3):e90972, 2014.

[26] RA Barrio, C Varea, JL Aragón, and PK Maini. A two-dimensional numerical study of spatial pattern formation in interacting turing systems. *Bulletin of mathematical biology*, 61(3):483–505, 1999.

[27] JL Aragón, RA Barrio, TE Woolley, RE Baker, and PK Maini. Nonlinear effects on turing patterns: Time oscillations and chaos. *Physical Review E*, 86(2):026201, 2012.

Certificate Of Completeness

It is hereby certified that the dissertation submitted by NS Ahsan Naseer, Reg No. **00000317712**, Titled as **Nonlinear Analysis of BVAM Model using Perturbation Techniques** has been checked, reviewed and its contents are complete in all respects.

Supervisor's Name: **Dr. Imran Akhtar** Signature: _____

Date: _____